Geochimica et Cosmochimica Acta 401 (2025) 17–30

Contents lists available at ScienceDirect

Geochimica et Cosmochimica Acta

journal homepage: www.elsevier.com/locate/gca

Germanium isotope fractionation during evaporation from metal and sulfide melts: Implications for volatile element loss from planetary materials

Elias Wölfer [a,b,*], Christian J. Renggli [a,c], Christoph Burkhardt [a,b], Thorsten Kleine [a,b]

[a] Max Planck Institute for Solar System Research, Justus-von-Liebig-Weg 3, 37077 Göttingen, Germany
[b] Institut für Planetologie, University of Münster, Wilhelm-Klemm-Straße 10, 48149 Münster, Germany
[c] Institut für Mineralogie, University of Münster, Corrensstr. 24, 48149 Münster, Germany

ARTICLE INFO

Associate editor: Béatrice Luais

Keywords:
Germanium
Degassing experiments
Non-magmatic iron meteorites
Stable isotope fractionation
Evaporation
Volatile depletion
Moderately volatile elements

ABSTRACT

The Ge elemental and isotopic composition of planetary materials holds essential clues on volatile element fractionation processes in nebular and planetary environments. To facilitate the interpretation of natural sample data we report the results of an experimental campaign that quantitatively assesses the elemental and isotopic fractionation of Ge during evaporation from graphite saturated Fe metal and FeS sulfide melts. The experiments were run under reducing conditions both at atmospheric and low vacuum (~0.001 bar) pressure and at temperatures between 1200–1600 °C. In general, evaporation of Ge increases with increasing temperatures, decreasing pressure, and in the presence of S. The residual run products become isotopically heavier with ongoing evaporation of Ge, yielding kinetic fractionation factors α_k between 0.9940 and 0.9971 for the Fe melt degassing series performed under low vacuum and atmospheric pressure, respectively.

The experimental data are applied to investigate the role of planetary degassing processes for setting the moderately volatile element budget of non-magmatic iron meteorites. For this, new Ge concentration and isotope data for ungrouped iron meteorites of non-magmatic origin are combined with literature data for group IAB and IIE irons. We find that the large Ge isotopic variations (~4‰) among variably Ge-depleted, non-magmatic iron meteorites are well explained by evaporative Ge loss from Fe metal or FeS sulfide melts at pressure conditions ≤ 1 bar. This supports models proposing an origin of non-magmatic iron meteorites by near-surface impact processes.

1. Introduction

Meteorites and other planetary materials are characterized by highly variable abundances of volatile elements (e.g., Palme and O'Neill, 2014; Braukmüller et al., 2018; Alexander, 2019a,b; Lodders, 2021). This equally applies to siderophile (i.e., 'metal-loving'), chalcophile (i.e., 'sulfide-loving'), and lithophile (i.e., 'silicate-loving') elements and, thus, represents a ubiquitous process during the early stages of Solar System evolution (e.g., Larimer and Anders, 1967; Alexander, 2005; Davis, 2006; Albarède, 2009; Hans et al., 2013). Iron meteorites in particular display highly variable (siderophile/chalcophile) volatile element contents and sample some of the most volatile-rich and −depleted planetary materials known (Wasson, 1967, 1970; Davis, 2006). Yet, it remains debated to which extent these depletions are inherited from a bodies' precursor materials, and how much is related to subsequent volatile loss after parent body accretion (Mittlefehldt, 1987; Cassen, 1996; Hin et al., 2017; Hirschmann et al., 2021; Nie et al., 2021; Hu et al., 2022; Grewal et al., 2025).

Germanium is a moderately volatile element (MVE) with a 50 % condensation temperature (T_C) from a gas of solar composition of 883 K (Wood et al., 2019; Lodders, 2021), and occurs in different valence states in geo-/cosmochemical environments: Ge^0 in metals, Ge^{2+} in sulfides, and Ge^{4+} in silicates and oxides. These attributes make Ge elemental and isotopic fractionation a key tool for constraining nebular and planetary fractionation processes affecting MVE abundances (Luais, 2012; Rouxel and Luais, 2017; Florin et al., 2020). For instance, Ge concentrations among iron meteorites vary by several orders of magnitude, a feature that cannot be explained by fractional crystallization of

* Corresponding author at: Max Planck Institute for Solar System Research, Justus-von-Liebig-Weg 3, 37077 Göttingen, Germany.
E-mail address: woelfer@mps.mpg.de (E. Wölfer).

https://doi.org/10.1016/j.gca.2025.05.044
Received 4 December 2024; Accepted 28 May 2025
Available online 30 May 2025

metallic melts (Scott and Wasson, 1975; Wasson et al., 2007; Luais, 2007). On this basis, different iron meteorite groups have been defined based on the degree of Ge depletion, where samples from each iron meteorite group are characterized by relatively constant Ge concentrations, while there are large variations in Ge concentrations among the different groups (Scott and Wasson, 1975). Notable exceptions are the group IAB and IIE irons, which collectively are classified as 'non-magmatic' irons. Compared to the other iron meteorite groups (i.e., the 'magmatic' irons) these irons exhibit more variable Ge concentrations [i.e., ~1–500 μg/g for the IABs and ~50–80 μg/g for the IIEs (Wasson and Wang, 1986; Choi et al., 1995; Wasson and Kallemeyn, 2002; Wasson, 2017)], and have chemical compositions that cannot easily be explained by simple fractional crystallization of a metal melt. Hence, unlike the magmatic iron meteorites, which are thought to represent planetary core material, the non-magmatic irons are interpreted to have formed by local melting events related to impact heating in the near-surface regions of planetesimals (Wasson and Wang, 1986; Wasson and Kallemeyn, 2002; Wasson, 2017; Worsham et al., 2017; Kruijer and Kleine, 2019).

While the classification of iron meteorites based on Ge was established in the 1970s, the origin of the large variations in Ge (and other MVE) abundances among the iron meteorites, and the distinct systematics of magmatic and non-magmatic groups is still poorly understood. In general, MVE depletions may arise during heating processes in the solar protoplanetary disk (e.g., Larimer and Anders, 1967; Cassen, 1996; Hellmann et al., 2020; Nie et al., 2021), or result from large-scale magma degassing or vaporization during local, near-surface melting of the parent asteroids (Mittlefehldt, 1987; Hin et al., 2017; Jordan et al., 2019; Hirschmann et al., 2021). Information on such MVE depletion processes may be obtained by investigating mass-dependent isotope variations among meteorites, which are sensitive tracers of condensation and evaporation (Humayun and Clayton, 1995; Young et al., 2002; Dauphas and Schauble, 2016; Bourdon and Fitoussi, 2020). For instance, Luais (2007, 2012) found large mass-dependent Ge isotope variations among IIE iron meteorites, indicative of kinetic isotope fractionation during magma degassing, while magmatic irons tend to show more homogeneous Ge isotopic compositions, suggesting distinct MVE depletion mechanisms for magmatic and non-magmatic iron meteorites.

However, given the lack of empirical data on the (degassing) behavior of Ge in high-temperature conditions, a quantitative assessment of Ge loss processes affecting iron meteorites has until now not been possible. Controlled degassing experiments of MVEs from synthetic melts have gained increasing attention in the last years (Richter et al., 2007, 2009, 2011; Norris and Wood, 2017; Young et al., 2019; Wimpenny et al., 2019, 2020; Sossi et al., 2019, 2020; Nielsen et al., 2021; Neuman et al., 2022). They are particularly useful in the context of constraining MVE loss process from meteorite parent bodies when combined with an assessment of the magnitude and direction of any associated mass-dependent isotope fractionation. For instance, Renggli et al. (2022) and Klemme et al. (2022) experimentally determined the elemental and isotopic fractionation behavior of Te and Cr during evaporation from silicate melts at redox and temperature settings relevant to igneous processes in different Solar System settings, and thereby aided the interpretation of natural sample signatures. Likewise, Steenstra et al. (2023, 2024) investigated the evaporative behavior of siderophile MVEs from metal and sulfide melts and found that S exerts a strong control on the degassing behavior of the MVEs. Metal transport experiments along temperature gradients, and thermodynamic speciation calculations, have further shown the important effect of ligands such as S and Cl on the volatility of MVEs. Sulfur, in particular, can increase the volatility of Ge by orders of magnitude at a given temperature (Renggli and Klemme, 2020). However, besides these improvements, there is a scarcity of thermodynamic constraints on Ge evaporation, and experimentally-determined Ge isotope fractionation data for relevant systems are absent.

Here we investigate the coupled elemental and isotopic fractionation of Ge in controlled degassing experiments from Fe metal and FeS melts. The experiments are run under reducing conditions at atmospheric pressure (graphite-CO fO_2 buffer), and at low vacuum (~0.001 bar) and temperatures of 1200–1600 °C, and allow for the first time to quantitatively assess the elemental and isotopic fractionation of Ge in high-T settings. Ultimately, the results of our degassing experiments can be taken as proxies for quantifying the conditions of evaporative Ge loss from planetary materials. This will be exemplified for non-magmatic iron meteorites, where new Ge isotope data for ungrouped non-magmatic irons in combination with previously published Ge concentration and isotope data for IAB and IIE irons (Luais, 2007, 2012; Wölfer et al., 2025a), will be assessed with respect to degassing processes on their parent planetesimals.

2. Materials and Methods

2.1. Starting material and evaporation experiments

The Ge evaporation experiments were run with two compositions, (i) a Fe metal and (ii) a FeS sulfide melt that contained ~0.4 wt% Ge. At this concentration, Ge is in a dilute solution in the melts, such that Henry's law applies. The starting materials were prepared by doping high-purity powders of Fe and FeS with a high-purity powder of Ge, respectively, and by homogenizing these mixtures with a pestle in an agate mortar for 30 min (see Steenstra et al. (2023, 2024) for details). Aliquots (~100 mg) of these homogenized starting materials were placed in a home-made pellet press and compacted to form dense and stable metal/sulfide pellets (~3 mm diameter; ~5 mm height). As demonstrated by Steenstra et al. (2023), this procedure results in chemically homogeneous starting materials that do not show any evidence of zonation. In line with that, we digested two unprocessed pellets of the Fe starting material, and one pellet of the FeS starting material for Ge concentration measurements by isotope dilution, as well as stable Ge isotope analyses (see below), and found both chemical and isotopic homogeneity (3946 ±33 μg/g Ge, $\delta^{74/70}$Ge = –0.22±0.04 and 3950±33 μg/g Ge, $\delta^{74/70}$Ge = –0.18±0.04 for the Fe starting material #1 and #2, respectively, and 3953±36 μg Ge, –0.18±0.05 for the FeS starting material; Table 1).

The experimental setup was largely adapted from Steenstra et al. (2023). For each experimental run, two metal or sulfide pellets were loaded in separate graphite buckets (~3 mm inner diameter; ~5 mm outer diameter; ~1.5 cm height; small hole at the bottom for FeS experiments) that were placed next to each other in a single, larger graphite bucket (~1.2 cm inner diameter; ~1.6 cm outer diameter; ~4–5 cm height). A Re wire was used to suspend the larger graphite bucket in a sealable, vertical gas-mixing tube furnace (Gero GmbH) with a gas volume of ~1160 cm^3. Of the two metal/sulfide pellets run in parallel in each experiment, one was designated for image documentation using a JEOL 6510 LA scanning electron microscope (SEM) at the Institute for Mineralogy in Münster, and the other was digested for bulk Ge concentration and stable isotope measurements. Note that any two samples run in parallel always experienced the same experimental conditions (e.g., pressure, temperature, run duration, oxygen fugacity [fO_2]).

For the low vacuum experiments an Alcatel rotary vane vacuum pump was attached to the furnace, where the pressure was monitored using an Edwards vacuum gauge. Experiments at atmospheric pressure were conducted under a CO-gas flow of 100 cm^3/min, buffering the fO_2 at the graphite-CO buffer by placing the samples in graphite cups. The temperature was monitored using a type B thermocouple and a programmable Eurotherm 3508 controller. Iron metal experiments were conducted for 60 min both at atmospheric pressure (~1 bar, under CO-gas flow) and at low vacuum (~0.001 bar) at varying temperatures of ~1300–1600 °C. As the volatility of Ge dramatically increases in the presence of S (Renggli and Klemme, 2020; Steenstra et al., 2023), FeS experiments were conducted for only 5 min both at atmospheric pressure and at low vacuum as well as at lower temperatures of

Table 1
Germanium concentration and isotopic data for the experimental run products.

Lab-ID	T [°C]	Ge (μg/g)[a] (± 2σ)	'Ge loss' [c] (± 2σ)	log*f*(Ge) [d] (± 2σ)	–ln*f*(Ge) [e] (± 2σ)	N (Ge-ID)	$\delta^{74/70}$Ge (± 2σ)	$\Delta^{74/70}$Ge (± 2σ)
Starting compositions								
Fe starting #1		3946 ± 33				8	–0.22 ± 0.04	
Fe starting #2		3950 ± 33				10	–0.18 ± 0.04	
FeS starting		3953 ± 36				10	–0.18 ± 0.05	
Fe metal melt degassing series (1 bar, 60 min runtime)								
Fe No. 2	1300	1424 ± 22	0.639 ± 0.006	–0.443 ± 0.007	1.019 ± 0.016	10	1.66 ± 0.04	1.86 ± 0.05
Fe No. 4	1400	3599 ± 25	0.088 ± 0.008	–0.040 ± 0.004	0.093 ± 0.009	9	0.02 ± 0.09	0.22 ± 0.09
Fe No. 6	1450	2312 ± 20	0.414 ± 0.006	–0.232 ± 0.005	0.535 ± 0.011	10	0.56 ± 0.04	0.76 ± 0.05
Fe No. 7	1500	3008 ± 32	0.238 ± 0.009	–0.118 ± 0.005	0.272 ± 0.012	10	0.96 ± 0.03	1.16 ± 0.05
Fe No. 10	1550	2981 ± 32	0.245 ± 0.009	–0.122 ± 0.005	0.281 ± 0.012	10	0.84 ± 0.05	1.04 ± 0.06
Fe No. 12	1600	869.1 ± 8.7	0.780 ± 0.003	–0.657 ± 0.003	1.513 ± 0.012	10	4.65 ± 0.03	4.85 ± 0.04
Fe metal melt degassing series ('vacuum', ~0.001 bar, 60 min runtime)								
Fe No. 19	1300	727.2 ± 5.7	0.861 ± 0.002	–0.735 ± 0.004	1.692 ± 0.010	9	7.49 ± 0.07	7.69 ± 0.07
Fe No. 21	1400	193.7 ± 2.1	0.951 ± 0.001	–1.309 ± 0.005	3.015 ± 0.012	9	18.13 ± 0.04	18.33 ± 0.05
Fe No. 24	1450	1.8 [b]	1.000	–3.332	7.672			
Fe No. 18	1500	25.14 ± 0.29	0.9936 ± 0.0001	–2.196 ± 0.006	5.056 ± 0.013	9	31.51 ± 0.05	31.71 ± 0.06
Fe No. 15	1550	0.4 [b]	1.000	–4.038	9.298			
Fe No. 13	1600	1.0 [b]	1.000	–3.607	8.306			
FeS sulfide melt degassing series (1 bar, 5 min runtime)								
FeS No. 23	1200	349.9 ± 4.3	0.911 ± 0.001	–1.053 ± 0.007	2.425 ± 0.015	8	13.25 ± 0.04	13.43 ± 0.06
FeS No. 21	1250	26.16 ± 0.30	0.993 ± 0.001	–2.179 ± 0.006	5.018 ± 0.015	8	30.02 ± 0.05	30.20 ± 0.07
FeS No. 19	1300	11.2 [b]	0.997	–2.548	5.867			
FeS No. 18	1350	10.1 [b]	0.997	–2.593	5.971			
FeS No. 16	1400	1.1 [b]	1.000	–3.552	8.178			
FeS No. 14	1500	0.4 [b]	1.000	–4.046	9.316			
FeS sulfide melt degassing series ('vacuum', ~0.001 bar, 5 min runtime)								
FeS No. 2	1200	0.6 [b]	1.000	–3.801	8.752			
FeS No. 4	1250	0.4 [b]	1.000	–3.977	9.158			
FeS No. 5	1300	0.4 [b]	1.000	–3.978	9.160			
FeS No. 8	1350	0.4 [b]	1.000	–4.002	9.214			
FeS No. 9	1400	0.4 [b]	1.000	–3.955	9.106			
FeS No. 12	1500	0.6 [b]	1.000	–3.789	8.725			

The $\delta^{74/70}$Ge data of the individual samples are reported as the mean of pooled measurements and the corresponding uncertainties reflect Student-t 95% confidence intervals (95% CI). N: number of isotope analyses.

[a] Germanium concentrations as determined by isotope dilution.

[b] Germanium concentrations as determined by quadrupole ICP–MS, which have an uncertainty of ~5 %. The measurements were performed just after sample digestion. These samples have not been further processed through the analytical protocol and no Ge stable isotope compositions were determined.

[c] Ge loss expressed as $1–([Ge]_{residue}/[Ge]_{initial})$.

[d] Ge loss expressed as $\log([Ge]_{residue}/[Ge]_{initial})$.

[e] Ge loss expressed as $–\ln([Ge]_{residue}/[Ge]_{initial})$.

~1200–1500 °C.

It was shown by Steenstra et al. (2023, 2024) that at the chosen experimental conditions the low viscosities of the Fe and FeS melts allow for a homogenous distribution of Ge throughout the melt. Therefore, the experimental run products reflect evaporative Ge loss (i.e., Ge degassing) not limited by diffusion within the Fe and FeS melts. Finally, after each experimental run, the samples were quenched in water and the respective pellets for image documentation were embedded in epoxy resin, polished, and carbon-coated.

2.2. Sample characterization by scanning electron microscopy

Back-scattered electron (BSE) images of the experimental run products were obtained using a JEOL 6510 LA scanning electron microscope (SEM) set to an acceleration voltage of 20 kV and a working distance of 10 mm. Most run products consisted of a single, quenched metal or sulfide spherule with a typical diameter of ~2–3 mm (Fig. 1). A variety of distinct quenching textures are present, including holes, exsolution lamellae of different Fe(-C) phases like austenite, ledeburite, and ferrite for the Fe melt experiments, and quenching-related fractures for the FeS melt experiments. All these textures are indicative of fully molten samples at the time of quenching, consistent with predictions from Fe-S-C phase diagrams on C-saturated Fe and FeS liquids (Lord et al., 2009; Buono and Walker, 2011). Saturation of C in the melts is evidenced by the presence of small graphite inclusions in all quenched samples (Fig. 2). In addition, FeS experiments (especially the ones degassed under low vacuum conditions) also display extensive depletions of S with increasing run temperatures, leading to the immiscibility of a S-rich, C-poor FeS melt and a S-poor, C-rich Fe melt (Steenstra et al., 2023) (Fig. 2). This observation is in agreement with phase equilibrium predictions (e.g., Corgne et al., 2008).

2.3. Natural samples

We report new Ge concentration and stable isotope data for four ungrouped iron meteorites from the non-carbonaceous (NC) meteorite reservoir (Spitzer et al., 2025). These include the potentially co-genetic irons Butler and NWA 859, which are the most Ge-rich iron meteorites known (i.e., >2000 μg/g Ge; Wasson, 1966, 2011; Spitzer et al., 2025). Further, we present data on two Ge-depleted irons, Washington County (~20 μg/g Ge) and Cambria (~1–2 μg/g Ge) (Wasson and Schaudy, 1971). At least for Butler, NWA 859, and Cambria, there is chemical and

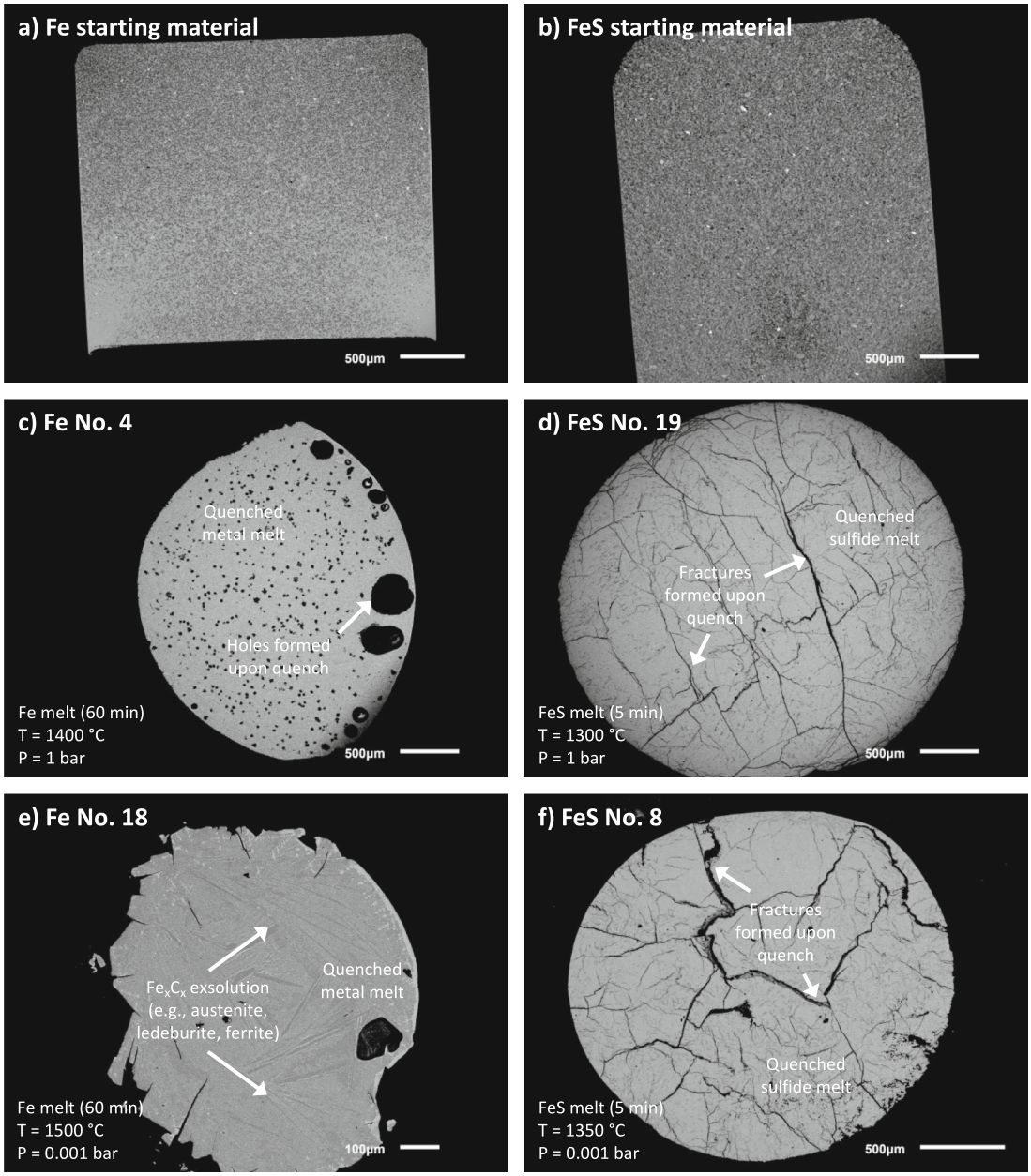

Fig. 1. Backscattered electron (BSE) images of polished cross-sections of the (a) Ge-Fe and (b) Ge-FeS starting materials (i.e., compacted metal/sulfide pellets) and typical experimental run products: (c) Metal melt degassing experiment at 1 bar, (d) sulfide melt degassing experiment at 1 bar, (e) metal melt degassing experiment at 0.001 bar (i.e., low vacuum), (f) sulfide melt degassing experiment at 0.001 bar.

isotopic evidence for non-magmatic origins (Wasson, 2011; Spitzer et al., 2025). By contrast, petrological, chemical, and isotopic evidence for Washington County is too sparse to assign either a magmatic or non-magmatic origin. In addition, we also analyzed three samples of the non-magmatic IAB iron meteorite group (Canyon Diablo, Odessa, Landes) and two samples of the non-magmatic IIE iron meteorite group (Miles, Weekeroo Station). The latter data have been reported in Wölfer et al. (2025a), and are interpreted within this study.

2.4. Sample preparation and chemical separation of Ge

Starting materials and experimental run products designated for Ge stable isotope measurements were cleaned with ultrapure water and ultrasonicated in ethanol for 5 min to remove adhering graphite particles from the experimental bucket. For the non-magmatic iron meteorites, ~40–200 mg pieces were cut from larger hand specimens using a diamond saw. Care was taken to only sample unaltered and freshly looking pieces with a 'metallic' appearance. After polishing cutting surfaces with SiC, the iron meteorite samples were cleaned in an ultrasonic bath in ethanol for 15 min.

For all samples, the cleaned metal/sulfide pieces were individually weighed into 15 ml Savillex PFA vials and digested on a hotplate using concentrated HNO_3 at 120 °C for five days. After digestion, some sample solutions still contained finely dispersed graphite particles, which were removed after centrifuging the solutions. Afterwards, small aliquots (0.5 %) of the sample solutions were used for Ge concentration measurements using a Thermo Scientific XSeries II quadrupole inductively coupled plasma mass spectrometer (ICP-MS) in Münster. For the iron meteorites, Ni concentrations were determined as well.

Based on the concentrations obtained by these measurements, aliquots equivalent to ~1000 ng Ge (e.g., 0.25–100 % of the digested solutions, corresponding to 0.3–200 mg sample material) were taken from

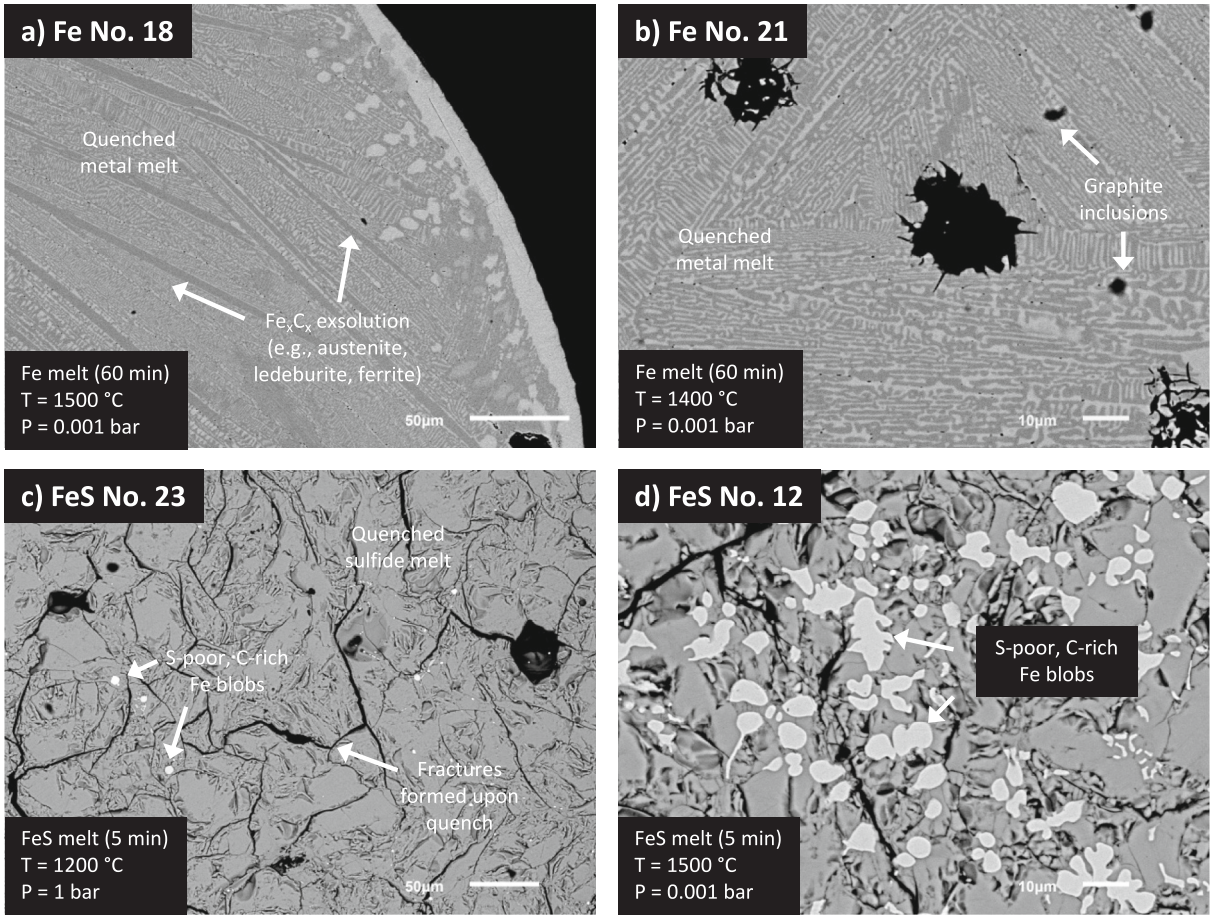

Fig. 2. Backscattered electron (BSE) images of polished cross-sections of experimental run products showing typical quench textures: (a, b) Metal melt degassing experiments displaying exsolution lamellae and abundant graphite inclusions. (c, d) Sulfide melt degassing experiments displaying quenching fractures. For some FeS experiments degassing of S was sufficiently high to result in immiscible S-poor, C-rich and S-rich, C-poor Fe liquids.

the sample solutions, mixed with appropriate amounts of a ^{70}Ge–^{73}Ge double-spike (Wölfer et al., 2025a), and equilibrated on a hotplate for ~24 h at 120 °C. Finally, the spiked sample solutions were dried down twice and re-dissolved in 0.5 M HNO_3 for ion exchange chromatography. To verify that the addition and equilibration of the Ge double spike only after the initial digestion step do not compromise the Ge concentration and isotope measurements (see below), we also digested four different pieces of the IC iron meteorite Arispe, two of which were spiked prior to sample digestion and two of which were spiked only after sample digestion, analogously to the degassing experiments and non-magmatic iron meteorites.

Germanium was then separated from the Fe(-Ni) matrix of the iron meteorites and the Fe(-S) matrix of the degassing experiments via a single-stage cation exchange chemistry, following previously described protocols (Luais, 2007, 2012; Florin et al., 2020, 2021; Wölfer et al., 2025a). In brief, samples were loaded in 2 mL 0.5 M HNO_3 onto Bio-Rad columns filled with 2 mL of pre-cleaned and conditioned Bio-Rad AG 50 W-X8 cation exchange resin (200–400 mesh), and Ge was directly eluted by additional 8 mL 0.5 M HNO_3, whereas Fe (and Ni) remained on the resin. Note that the capacity of 2 mL AG 50 W-X8 resin is equivalent to only ~60 mg Fe, hence, larger sample aliquots (e.g., Cambria) were dissolved in appropriate, larger volumes of 0.5 M HNO_3 and split on separate columns. The final (re-combined) Ge cuts were evaporated to dryness, repeatedly dried down in concentrated HNO_3, and then re-dissolved in 2 mL 0.5 M HNO_3 for the Ge isotope measurements. The Ge yields were >95 % and the total procedural blank was <1 ng and, thus, negligible for all samples.

2.5. Germanium isotope measurements

The Ge isotope measurements were performed on a Thermo Scientific Neptune *Plus* multicollector ICP-MS at the Institute for Planetology in Münster, following the analytical protocol of Wölfer et al. (2025a). Samples were introduced using a Cetac Aridus II desolvator and a Savillex C-flow nebulizer at an uptake rate of ~70 µl/min. Using standard sampler and X skimmer cones, a signal intensity of ~10 V on ^{70}Ge was obtained for an optimally spiked ~100 ppb Ge solution. Each analysis was composed of on-peak zero measurements of 20 × 8 s, followed by 50 isotope ratio measurements of 8 s each. Isobaric interferences of Zn on ^{70}Ge and of Se on ^{74}Ge and ^{76}Ge were corrected by monitoring ^{68}Zn and ^{77}Se and using the exponential mass fractionation law. Prior to each analysis, the sample introduction system was rinsed for 5 min using 0.28 M HNO_3. Processing of the measured raw data was performed off-line following the three-dimensional data reduction scheme of Siebert et al. (2001), as described by Wölfer et al. (2025a). The isotope composition data are reported in $\delta^{74/70}$Ge notation relative to the NIST SRM 3210a Ge standard:

$$\delta^{74/70}Ge = \left[\frac{\left({}^{74}Ge/{}^{70}Ge \right)_{sample}}{\left({}^{74}Ge/{}^{70}Ge \right)_{SRM3120a}} - 1 \right] \times 1000 \quad (1)$$

and for each sample represent the mean of replicate measurements and the corresponding errors are Student-t 95 % confidence intervals (95 % CI). For the spiked samples precise bulk Ge concentrations were determined by isotope dilution (Stracke et al., 2014).

The accuracy and reproducibility of the Ge concentration and isotope

measurements were assessed by repeated analyses of the Alfa Aesar Ge solution standard, which was processed through the chemical separation procedures together with the samples. The measured Ge isotopic composition of the Alfa Aesar Ge solution standard is $\delta^{74/70}$Ge = –0.77 ±0.03 (95 % CI, 2 s.d. = 0.08, N = 11), in excellent agreement with previously reported results (Wölfer et al., 2025a). Furthermore, the Arispe samples spiked at different times show indistinguishable Ge concentrations and isotopic compositions (e.g., ~240 ppm Ge; $\delta^{74/70}$Ge ≈ 0.9; Table 2), implying that Ge is neither lost nor isotopically fractionated during the sample digestion stage. Moreover, three IAB and two IIE iron meteorites (Wölfer et al., 2025a) processed in the analytical campaign along with the samples of this study agree very well with previously reported data for these iron meteorite groups (Luais, 2007, 2012), and thus further testify to the accuracy and reproducibility of our analytical protocol.

3. Results

3.1. Degassing experiments

Germanium concentrations and stable isotope variations of the experimental starting materials and residual run products are listed in Table 1 and shown in Fig. 3 and Fig. 4. The Ge stable isotope variations of the experiments are presented in $\Delta^{74/70}$Ge notation relative to the isotopic composition of the Fe (or FeS) starting material:

$$\Delta^{74/70}Ge = \delta^{74/70}Ge_{residue} - \delta^{74/70}Ge_{initial} \quad (2)$$

where $\delta^{74/70}Ge_{initial}$ is –0.20±0.03 for the Fe starting material (weighted mean calculated using IsoplotR, N = 2) and –0.18±0.05 for the FeS starting material (Table 1), and $\delta^{74/70}Ge_{residue}$ is the Ge stable isotope composition of the respective Ge evaporation experiment. Similarly, we define the depletion of Ge in the residual run products relative to the composition of the starting material as log*f*(Ge), where $f(Ge) = [Ge]_{residue}/[Ge]_{initial}$, and where $[Ge]_{initial}$ is 3948±23 µg/g for the Fe starting material (weighted mean calculated using IsoplotR, N = 2) and 395±36 µg/g for the FeS starting material, and $[Ge]_{residue}$ is the Ge concentration of the respective Ge evaporation experiment.

We performed four degassing series consisting of six individual runs each (i.e., 24 experimental runs in total). The melt compositions, experimental run time, oxygen fugacity, and pressure conditions were constant within each series, but temperatures were varied for each of the six experimental runs (Table 1). For all four degassing series we observe that the magnitude of Ge stable isotope fractionation (i.e., $\Delta^{74/70}$Ge) increases with increasing loss of Ge [i.e., decreasing log*f*(Ge)] (Fig. 3). This behavior is expected, given that lighter isotopes have a higher zero-point energy and react faster in kinetic processes like evaporation (Dauphas and Schauble, 2016).

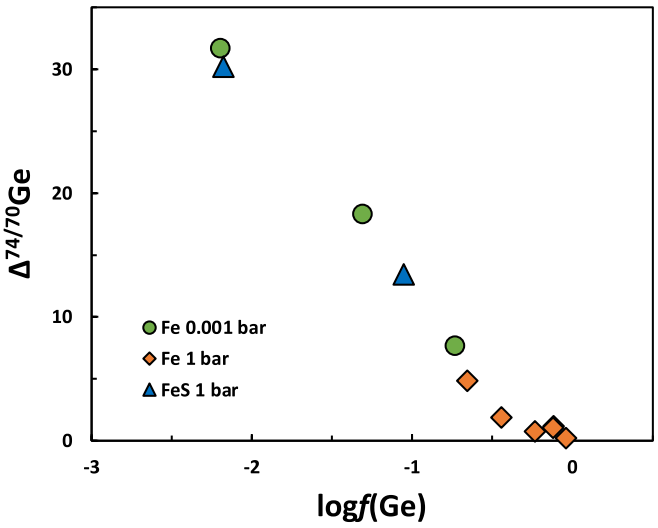

Fig. 3. Results from the Ge degassing experiments run between 1200–1600 °C (see Table 1 and Fig. 4 for details). The Ge content in each residual run product is stated relative to the initial Ge content of the respective starting composition [i.e., log*f*(Ge) = log($[Ge]_{residue}/[Ge]_{initial}$)].

Overall, log*f*(Ge) of the experiments varies from –0.04 to –4, corresponding to absolute Ge concentrations from 3599±25 µg/g to <0.4 µg/g, and a loss of ~9 % up to ~99.99 % of the initial Ge. In line with prior observations (Steenstra et al., 2023, 2024) the magnitude of Ge loss varies considerably between the different degassing series. Whereas samples of the Fe metal melt degassing series performed at atmospheric pressure display a large range of Ge depletions (e.g., ~9–80 %), all samples of the Fe metal melt degassing series performed under low vacuum conditions exhibit more pronounced Ge depletions (e.g., ~85–99.99 %), thus, illustrating that the magnitude of Ge loss [i.e., decreasing log*f*(Ge)] increases with decreasing pressure. Beyond that, log*f*(Ge) also decreases within each series with increasing run temperatures (Fig. 4**a**). This becomes evident in particular for the Fe metal melt degassing series performed under low vacuum conditions and the FeS

Table 2
Germanium concentration and isotopic data for ungrouped iron meteorites, the Arispe (IC) iron meteorite, and the Alfa Aesar Ge solution standard.

Sample	Ge (µg/g) (± 2σ)	Ni (wt%)	$(Ge/Ni)_{CI}$	N (Ge-ID)	$\delta^{74/70}$Ge (± 2σ)
Ungrouped irons					
Butler	1915 ± 20	16.0	3.9	7	0.96 ± 0.04
NWA 859	2358 ± 25	17.3	4.4	6	0.81 ± 0.05
Washington County	26.66 ± 0.31	10.0	0.087	6	2.74 ± 0.05
Cambria	1.690 ± 0.017	10.4	0.0053	6	3.12 ± 0.05
Ge double spike tests					
Arispe #1 (spiked prior to digestion)	244.2 ± 3.5	6.2	1.28	11	0.91 ± 0.03
Arispe #2 (spiked prior to digestion)	244.2 ± 3.5	6.2	1.28	12	0.86 ± 0.01
Arispe #3 (spiked after digestion)	236.1 ± 3.8	6.2	1.23	12	0.89 ± 0.02
Arispe #4 (spiked after digestion)	236.2 ± 2.5	6.2	1.23	7	0.89 ± 0.05
Solution standard					
Alfa Aesar				11	–0.77 ± 0.03

The $\delta^{74/70}$Ge data of the individual samples are reported as the mean of pooled measurements and the corresponding uncertainties reflect Student-t 95 % confidence intervals (95 % CI). N: number of isotope analyses. Germanium concentrations were determined by isotope dilution, Ni concentrations were determined by quadrupole ICP–MS, which have an uncertainty of ~ 5 %. The Ge/Ni ratios were normalized to the average ratio of CI chondrites (i.e., Ge/Ni = 30.8411; Wasson and Kallemeyn, 1988).

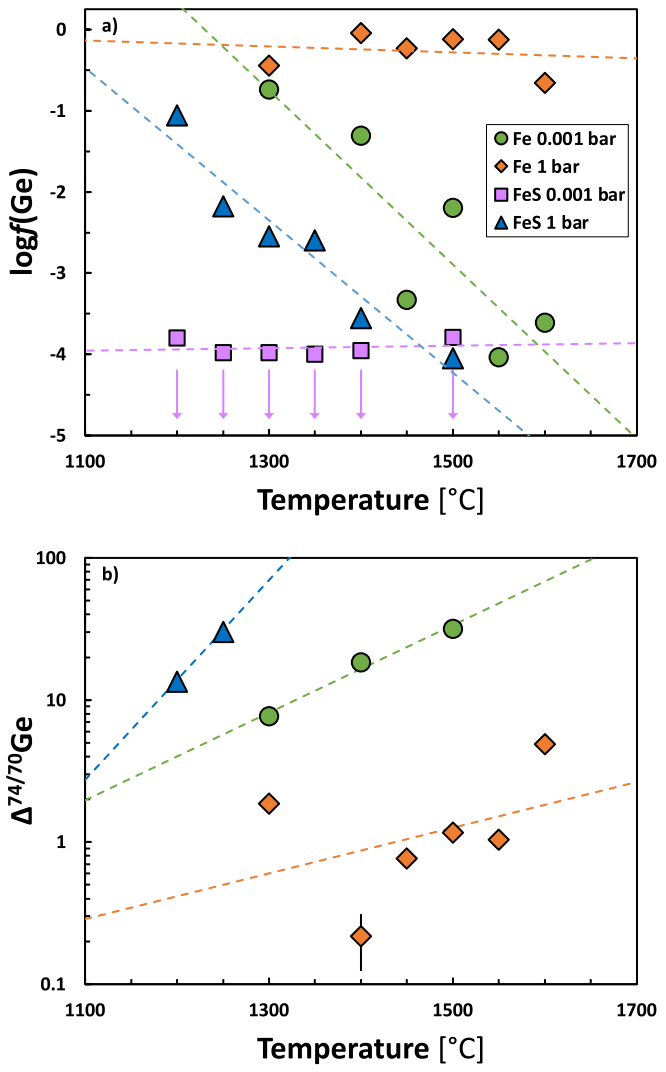

Fig. 4. Evaporative Ge loss (a) and Ge stable isotope fractionation (b) as a function of experimental run temperature. The Ge content in each residual run product is stated relative to the initial Ge content of the respective starting composition [i.e., log*f*(Ge) = log([Ge]$_{residue}$/[Ge]$_{initial}$)]. The Ge concentrations of the FeS run products degassed at low vacuum conditions (pink diamonds) were close to or below the detection limit of our quadrupole ICP–MS measurement routine and only represent maximum concentrations [see pink arrows in (a)].

melt degassing series performed at atmospheric pressure. For the FeS melt degassing series performed under low vacuum conditions this coherence is not quite clear, since all six runs of this series are characterized by extreme Ge depletions >99.9 % (i.e., close to or below the detection limit of our ICP–MS measurement routine; see Fig. 4**a**). In any case, our experimental results confirm that the presence of S in the melt drastically increases the evaporative loss of Ge. All residual FeS run products are characterized by Ge depletions >99 %, irrespective of temperature. The only exception is the sample FeS No. 23, which is the product of the lowest temperature (i.e., 1200 °C) run at atmospheric pressure, and shows a Ge depletion of ~91 %. The Fe metal melt degassing series performed at atmospheric pressure shows a poor correlation of Ge loss with increasing temperatures. Nevertheless, this behavior does not influence the strong relation of increasing $\Delta^{74/70}$Ge with decreasing log*f*(Ge) of the run products of this series (Fig. 3).

The total range of $\Delta^{74/70}$Ge displayed by the degassing experiments is ~31.5 ‰ (i.e., ~8‰/amu), with the minimum fractionation being 0.24 ‰ for the low temperature run (Fe No. 4) in the Fe metal melt degassing series at atmospheric pressure, and the maximum fractionation recorded in the Fe melt degassed into low vacuum (Fe No. 18). The latter sample lost 99.4 % of the initial Ge. Note that more extreme Ge isotope fractionations would be expected for samples which lost even more of their initial Ge (e.g., most of the residual run products of the FeS degassing series), however, no isotope composition data was obtained for these samples, due to the analytical challenges imposed by their low Ge contents (Table 1).

3.2. Ungrouped iron meteorites

The Ge abundances, Ge/Ni ratios, and $\delta^{74/70}$Ge compositions of the ungrouped, potentially non-magmatic iron meteorites of this study are listed in Table 2 and shown in Fig. 5. In addition, Ge concentration and isotopic data for the Ge Alfa Aesar solution standard and the Ge double spike tests on four different digestions of Arispe are listed in Table 2**.** The four ungrouped iron meteorites show highly variable Ge concentrations (and Ge/Ni) and isotopic compositions that do not fall within the range of any of the major magmatic and non-magmatic iron meteorite groups (Scott and Wasson, 1975; Luais, 2007, 2012; Wölfer et al., 2025a). The Ge concentrations as determined by isotope dilution are consistent with literature data previously published for these samples (Wasson, 1966, 2011; Wasson and Schaudy, 1971).

Butler and NWA 859 are the most Ge-rich iron meteorites at present (i.e., >2000 µg/g Ge; Ge/Ni$_{CI}$ ≈ 4) and exhibit $\delta^{74/70}$Ge compositions ($\delta^{74/70}$Ge = 0.96±0.04 for Butler and $\delta^{74/70}$Ge = 0.81±0.05 for NWA 859) within the range typically observed for most major (NC) magmatic iron meteorite groups [e.g., $\delta^{74/70}$Ge ≈ 0.8–1.2 (Luais, 2007, 2012; Wölfer et al., 2025a)] (Fig. 5).

By contrast, Washington County ($\delta^{74/70}$Ge = 2.74±0.05) and Cambria ($\delta^{74/70}$Ge = 3.12±0.05) display heavier Ge isotopic compositions (Fig. 5) than the magmatic iron meteorites. In fact, these two meteorites represent the isotopically heaviest meteorite samples measured to date. Interestingly, despite their similar Ge isotopic compositions, Washington County is characterized by 26.7±0.3 µg/g Ge (Ge/Ni$_{CI}$ ≈ 0.1) and, thus, falls within the Ge elemental range of type III iron meteorites (e.g., IIIAB, IIIE), whereas, Cambria with 1.69±0.02 µg/g Ge (Ge/Ni$_{CI}$ ≈ 0.005) is strongly depleted.

4. Discussion

4.1. Germanium isotope fractionation in controlled metal/sulfide melt degassing experiments

As demonstrated in prior studies (Steenstra et al., 2023, 2024), the homogenous distribution of Ge throughout both the Fe and FeS melts is promoted by their very low viscosities and, hence, no diffusion gradients were observed along concentration profiles through the experimental run products at the high temperature conditions investigated here (e.g., >1200 °C for the FeS runs and >1300 °C for the Fe runs; see section 2.1 for details). Therefore, the rate of Ge evaporation from the melts in the experimental run products is controlled only by the respective evaporation reactions, and not limited by the diffusion of Ge within the Fe and FeS melts. We suggest that the predominant evaporation reaction of Ge in the Fe melt system at reducing conditions (~C-CO buffer) at 1 bar and in low vacuum is $Ge_{(l)} \rightarrow Ge_{(g)}$. Evaporation of Ge as $Ge_{(g)}$ under reducing and oxygen-free conditions is likely analog to the gas-phase speciation of other metals under reducing conditions, including Zn, Ga, or Cu (Renggli et al., 2017). Evaporation of Ge as Ge_2 [e.g., $2Ge_{(l)} \rightarrow Ge_{2(g)}$], as Ge-oxide [e.g., $Ge_{(l)} + CO_{(g)} \rightarrow GeO_{(g)} + C_{(l/s)}$], or as Ge-carbide [e.g., $Ge_{(l)} + 2C_{(s)} \rightarrow GeC_{2(g)}$] is likely less relevant at these conditions, whereas $GeO_{(g)}$ would be the prevalent gas species in the presence of oxygen (Sossi et al., 2019; Lamoreaux et al., 1987). For the FeS melt system, the total vapor pressure is generally larger compared to the Fe melt system. Based on previous work investigating the Ge gas speciation in S-bearing systems (Renggli and Klemme, 2020; Wai and

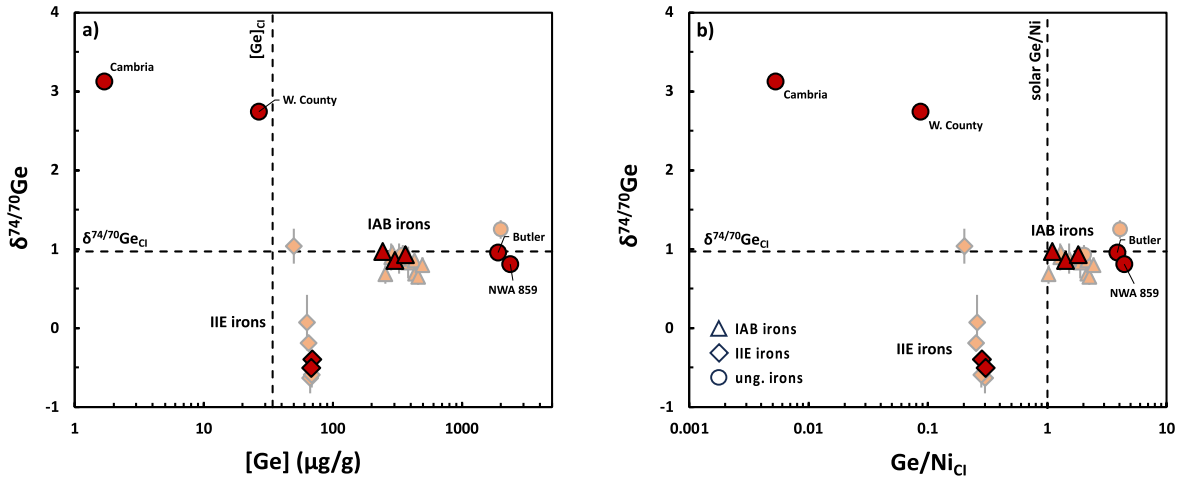

Fig. 5. Diagram of $\delta^{74/70}$Ge vs. Ge concentrations (a) or the CI-normalized Ge/Ni ratios (b) of the ungrouped, potentially non-magmatic iron meteorites of this study and the non-magmatic IAB and IIE iron meteorite groups. Data for the ungrouped irons Butler, NWA 859, Washington County (W. County), and Cambria (red circles) are from this study. Three IAB irons (red triangles) and two IIE irons (red diamonds) are from Wölfer et al. (2025a). Literature data (light red) for IAB irons, IIE irons, and ungrouped irons are from Luais (2007, 2012), Escoube et al. (2012), Wasson and Wang (1986), Choi et al. (1995), Wasson and Kallemeyn (2002), and Wasson (2017). Dotted lines illustrate the Ge concentration (or Ge/Ni) and isotopic composition of CI chondrites (Wasson and Kallemeyn, 1988; Wölfer et al., 2025b; Luais et al., 2022).

Wasson, 1979), we suggest that the predominant evaporation reaction of Ge in the FeS melt system at reducing conditions (~C-CO) at 1 bar and in low vacuum is $GeS_{(l)} \rightarrow GeS_{(g)}$. Similar to the Fe melt system, we suggest that other evaporation reactions are less relevant, including the evaporation of Ge as metallic Ge [e.g., $GeS_{(l)} \rightarrow Ge_{(g)} + S_{(g)}$], or as oxide [e.g., $GeS_{(l)} + CO_{(g)} \rightarrow Ge_{(g)} + COS_{(g)}$].

Consequently, we can calculate kinetic isotopic fractionation factors α_k for the evaporation of Ge and GeS from the Fe and FeS melts under reducing conditions, respectively. For each degassing series, the $\Delta^{74/70}$Ge of the individual run products increase with decreasing Ge concentrations, such that they define a linear array in a diagram of 1000ln(R/R_0) vs. –ln$f$(Ge), where 1000ln(R/R_0) is defined as follows:

$$1000 \times \ln(R/R_0) = 1000 \times \ln\left[\frac{\left(1 + 10^{-3} \times \Delta^{74/70}Ge_{residue}\right)}{\left(1 + 10^{-3} \times \Delta^{74/70}Ge_{initial}\right)}\right] \quad (3)$$

Such linear arrays are expected in the case of Rayleigh fractionation and their slopes are equal to 1000(1–α_k) (Renggli et al., 2022; Fig. 6). Thus, α_k of the evaporation of Ge and GeS from the Fe and FeS melts, respectively, is proportional to the slope of the isotopic data of the experiments (i.e., $\Delta^{74/70}$Ge) relative to the degree of volatile loss [i.e., log$f$(Ge)] as shown in Fig. 3.

Theoretic constraints on the kinetic behavior of gases indicate that the ratio of the effusion rates of two gases is the square root of the inverse ratio of their molar masses (i.e., Graham's law). This principle applies for the pinhole diffusion of a gas into a fully evacuated space. Accordingly, heavier gases diffuse more slowly than lighter gases. In the case of our degassing experiments, this causality implies that the rate of evaporating $^{74}Ge(S)_{(g)}$ is lower than that of $^{70}Ge(S)_{(g)}$, therefore, causing isotope fractionation by diffusion. Graham's law of diffusion (into a perfect vacuum) provides the theoretical maximum rate of isotope fractionation as a function of evaporative Ge loss in our degassing experiments (i.e., the theoretical $Ge(S)_{(g)}$ diffusion limit; Fig. 6 and Fig. 7). For the considered masses of ^{70}Ge and ^{74}Ge, a kinetic isotopic fractionation factor α_k of $(70/74)^{0.5} = 0.9726$ can be calculated for the Fe melt system with $Ge_{(g)}$ as the dominant gas phase species, which equals to a slope of 27.40 in a diagram of 1000ln(R/R_0) vs. –ln$f$(Ge). By contrast, in the case of the FeS melt system and $GeS_{(g)}$ being the dominant gas phase species, α_k is calculated as $(102/106)^{0.5} = 0.9810$, which equals to a slope of 19.05 in a diagram of 1000ln(R/R_0) vs. –ln$f$(Ge). Whereas these α_k-values correspond to the maximum possible, kinetic isotope fractionation between $^{70}Ge(S)$ and $^{74}Ge(S)$ during evaporation, an α_k-value of 1 would correspond to no isotope fractionation during evaporation [i.e., equal effusion rates of $^{70}Ge(S)$ and $^{74}Ge(S)$].

For our different degassing series, we obtained 0.9726 (and 0.9810) $< \alpha_k < 1$. Qualitatively consistent with theoretical constraints, the largest $\alpha_k = 0.9971$ (i.e., closest to $\alpha_k = 1$) is obtained for the Fe melt degassing series performed at atmospheric pressure (1 bar) (Fig. 6). By contrast, a smaller $\alpha_k = 0.9940$ is obtained for the Fe melt degassing series performed under low vacuum conditions (0.001 bar). This value is closer to the theoretical α_k-limit of $Ge_{(g)}$ diffusion, demonstrating that the magnitude of kinetic Ge isotope fractionation is larger at lower pressure conditions. Nevertheless, even for our Fe melt degassing series performed at 0.001 bar, the obtained α_k is considerably larger than the theoretically predicted limit of kinetic isotope fractionation.

Previous studies using gas mixing furnace setups have found that recondensation reactions play an important role in degassing experiments, especially at 1 bar and low-vacuum conditions (e.g., Grossman et al., 2000; Richter et al., 2002, 2011). Within the framework of diffusion of evaporated gas species through the surrounding gas, Richter et al. (2011) and Young et al. (2022) showed that the effective isotope fractionation is not just dependent on the overall gas pressure and the geometry of the experimental design, but also highly dependent on the composition of the surrounding gas. Following the approach presented in Richter et al. (2002) (c.f. their Fig. 13) the Hertz-Knudsen equation can be used to model the effective isotopic fractionation factors for $^{70}Ge/^{74}Ge$, $^{70}GeO/^{74}GeO$, and $^{70}GeS/^{74}GeS$, expressed as α_k–1, during evaporation into CO gas. The results of this exercise are shown in Fig. 7. It can be seen that for appropriate choices of the coefficient γ (with $\gamma = 0$ representing 'perfect evaporation' and $\gamma = 1$ representing zero net evaporation) and the radius r of an evaporating melt spherule (see Grossman et al., 2000; Richter et al., 2002, 2009, 2011; Sossi et al., 2019 for details), the fractionation factors experimentally determined at 0.001 bar and 1 bar (black squares in Fig. 7) can be reasonably well matched by the calculations. This implies that the CO gas pressure indeed seems to exert a major control on the isotope fractionation in our evaporation experiments. Although a more quantitative assessment of the evaporation behavior of Ge would require experiments at high vacuum and evaporation from a freely suspended melt droplet, some qualitative observations can be made by comparing the results of the calculations and the experiments. First, the temperature of evaporation seems to have only a very limited effect on the resulting effective isotope

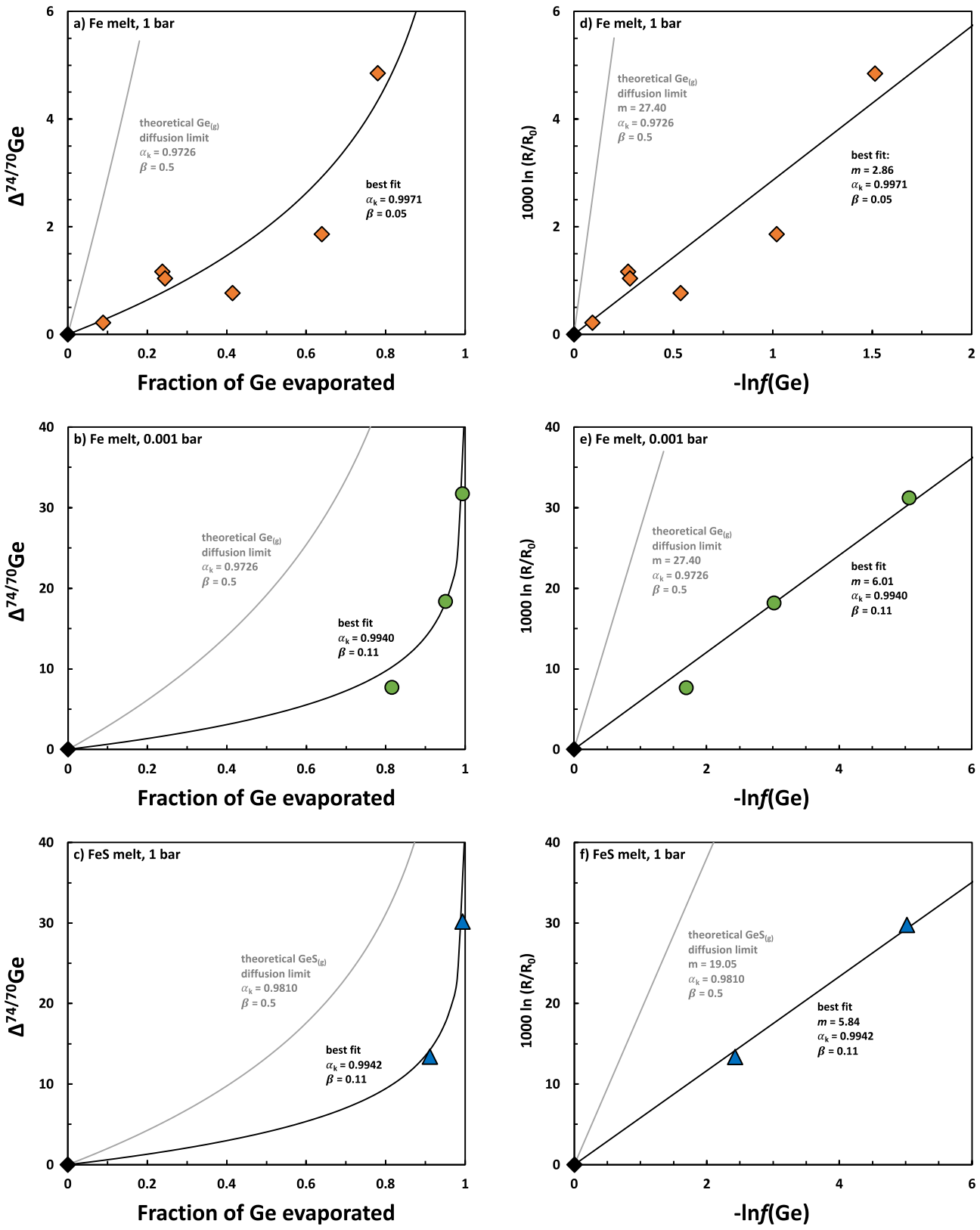

Fig. 6. Germanium stable isotope fractionation expressed as a function of Ge loss for (a) Fe metal melt degassing experiments at 1 bar (orange diamonds), (b) Fe metal melt degassing experiments at low vacuum (~0.001 bar; green circles), and (c) FeS sulfide melt degassing experiments at 1 bar (blue triangles). Black diamonds represent the experimental starting material and the black curves illustrate Rayleigh fractionation for evaporation of Ge from given starting compositions. In each of these cases, the kinetic fractionation factor α_k was calculated from the slope m of a linear best fit of the respective data in $1000\ln(R/R_0)$ vs. $-\ln f(Ge)$ space (panels d–f) as $\alpha_k = 1 - m/1000$. The stated β-values are fractionation exponents and they are related to α_k as follows: $\beta = \log(\alpha_k)/\log(m_{^{70}Ge(S)}/m_{^{74}Ge(S)})$. Grey curves/lines represent maximum Ge isotope fractionation according to Graham's Law ($\beta = 0.5$; $\alpha_k = 0.9726$ for the Fe melt system and $\alpha_k = 0.9810$ for the FeS melt system). Uncertainties are smaller than the symbol sizes.

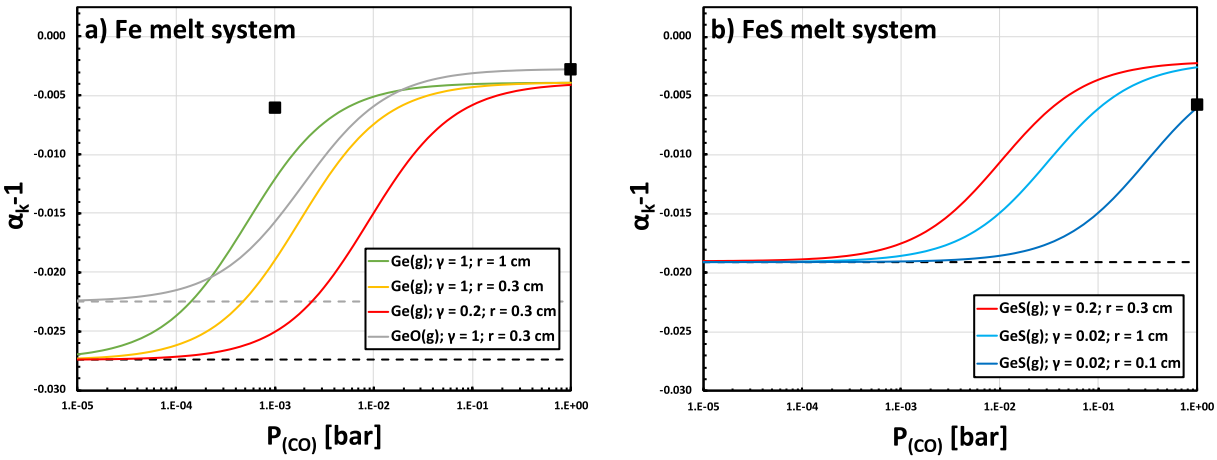

Fig. 7. Predicted effect of CO gas pressure on the Ge isotopic fractionation factors for evaporation of $Ge_{(g)}$ or $GeO_{(g)}$ from Fe melt (a) or $GeS_{(g)}$ from FeS melt (b). Dashed horizontal lines represent the respective theoretical diffusion limits. At higher CO pressures, the effective isotope fractionation factors deviate from the theoretical limits due to back-reactions. The experimentally constrained fractionation factors (black squares) can reasonably well be matched for appropriate choices of the coefficient γ (with $\gamma = 0$ representing 'perfect evaporation' and $\gamma = 1$ representing zero net evaporation) and the radius r of an evaporating melt spherule. In all modeled cases, the temperature was set to 1400 °C. See main text for details.

fractionation. The curves in Fig. 7 have been calculated for an evaporation temperature of 1400 °C, but would look similar for 1200 °C and 1600 °C. Second, in the case of evaporation of GeS from a sulfide melt, we find that calculated and experimentally measured isotope fractionation factors only coincide for very low γ (i.e., close to $\gamma = 0$; Fig. 7b). This might be consistent with the observation that the presence of S drastically increases the evaporation rate of Ge (e.g., >90 % Ge loss after only 5 mins run time). Lastly, the fractionation factor deduced for the Fe melt degassing experiments performed at 0.001 bar seems somewhat larger than the modeled ones, for a wide range of γ-values (e.g., $0 < \gamma \leq 1$), temperatures (e.g., 1200–1600 °C), reasonable radii of a hypothetical melt spherule (e.g., 0.1–0.3 cm), and irrespective of whether $Ge_{(g)}$ or $GeO_{(g)}$ are assumed as evaporative species (Fig. 7a). A good match can only be achieved for large γ (i.e., $\gamma \approx 1$) and large radii (e.g., $r > 3$ cm). This might indicate suppression of isotope fractionation due to a geometric effect in our setup, in addition to the CO pressure effect.

In our experiments the metal and sulfide melts were placed in graphite cups, limiting the extraction of the evaporated Ge from the sample, and likely promoting back reaction. Suspension of the melts on metal wires, as usually done for furnace experiments (e.g., Sossi et al., 2019; Renggli et al., 2022) with silicate melts was not possible, because the metal melts would alloy with the wires. Therefore, the surface from which evaporation could have taken place in our open top setup is lower compared to a suspended spherule. Furthermore, the flow of gas away from the evaporating sample surface might have been impeded, due to the geometry of the containers, causing a local enrichment in the density of gas molecules above the melt surface.

Interestingly, for the FeS melt degassing series performed at 1 bar, we obtained $\alpha_k = 0.9945$, which is very similar to that of the Fe melt degassing series performed at 0.001 bar. Therefore, the magnitude of Ge isotope fractionation is also increased by the presence of S in the melt. Overall, thus, lower pressure conditions and the presence of S in the melt enhance the evaporative loss of Ge (i.e., increasing Ge elemental depletion), and promote larger Ge isotope fractionations. As we did not obtain Ge isotopic data for experimental runs of the FeS melt degassing series at 0.001 bar, we cannot report an α_k for this series. Nevertheless, given that Ge was largely volatilized already in the low-temperature runs, we expect an α_k even smaller compared to the FeS melt degassing series performed at 1 bar (e.g., $\alpha_k < 0.9945$).

The calculated α_k-values of each degassing series can be used to quantitatively model the isotopic fractionation of Ge as a function of the evaporative Ge loss in turn. Assuming that the evaporation of Ge in our degassing experiments follows the principles of Rayleigh fractionation, $\Delta^{74/70}$Ge can be calculated for any Ge loss step as follows:

$$\Delta^{74/70}Ge = \left(\Delta^{74/70}Ge_{initial} + 1000\right) * \left([Ge]_{residue}/[Ge]_{initial}\right)^{(\alpha k - 1)} - 1000 \quad (4)$$

where $\Delta^{74/70}Ge_{initial}$ is 0 by definition (i.e., the $\Delta^{74/70}$Ge of the starting composition), $[Ge]_{residue}$ is any Ge concentration after Ge loss, $[Ge]_{initial}$ is the Ge concentration of each starting material (i.e., 3948±23 µg/g Ge for the Fe starting material and 3953±36 µg/g Ge for the FeS starting material), and α_k is the kinetic isotopic fractionation factor determined for each degassing series. In Fig. 6 we fitted our experimental data for each degassing series using our calculated α_k-values, and show the theoretical evolution the Ge isotopic fractionation as a function of the fraction of evaporated Ge for each degassing series. Altogether, these new experimental constraints on the evaporation behavior of Ge in high temperature settings help to better understand the role of melt degassing processes for setting the volatile element budget of (some) planetary building blocks (see below).

4.2. Germanium isotope fractionation in non-magmatic iron meteorites

4.2.1. The non-magmatic IAB and IIE iron meteorite groups

The non-magmatic IAB and IIE iron meteorite groups are characterized by more variable Ge concentrations than the magmatic iron groups (Scott and Wasson, 1975). The IAB irons in particular show Ge variations from as low as ~1 µg/g Ge up to >500 µg/g Ge (Choi et al., 1995; Wasson and Kallemeyn, 2002). Germanium and Ni are both siderophile and show a very similar partitioning behavior between metal and silicate (Luais, 2007; Palme and O'Neill, 2014). Consequently, the Ge/Ni is not significantly modified by core formation processes. By contrast, since Ni is non-volatile, Ge/Ni variations among iron meteorites likely reflect volatility-related Ge fractionation (Davis, 2006). However, thus far only IAB irons with super-chondritic Ge/Ni (i.e., with Ge enrichments above the solar value) have been analyzed. These samples show only limited to no $\delta^{74/70}$Ge variation (Luais, 2007, 2012; Wölfer et al. 2025a; see Fig. 5), implying that the process of Ge-enrichment in these samples was not accompanied by Ge isotope fractionation. As such, the results of our degassing experiments cannot directly be applied to these samples. A detailed assessment of the origin of MVE variations among IABs needs to await Ge isotopic analyses of samples with sub-chondritic Ge/Ni and should be a focus of future research.

Contrary to the IAB irons, the IIE iron meteorite samples show both, large-scale $\delta^{74/70}$Ge variations and Ge elemental depletions (i.e., sub-

chondritic Ge/Ni; Fig. 5). These elemental and isotopic variations are coupled, where increasingly Ge-depleted IIE irons show increasingly heavier $\delta^{74/70}$Ge compositions compared to the most Ge-rich IIE iron meteorite Miles (e.g., $\delta^{74/70}$Ge = –0.59; Luais, 2007, 2012; Wölfer et al. 2025a). These signatures were related to evaporative loss during impact heating processes (Luais, 2007). With the new experimental data from our metal/sulfide melt degassing series, we can assess this model more quantitatively. By interpreting the Ge elemental and isotopic variations of the IIE irons as degassing signatures, we can plot the IIE irons in a fashion analogous to our degassing experiments in diagrams of 1000ln (R/R_0) vs. –ln*f*(Ge), and $\Delta^{74/70}$Ge vs. the fraction of evaporated Ge (Fig. 8). In the former diagram, the IIE irons define a linear array with a slope of 5.29, which corresponds to $\alpha_k = 0.9947$ [and $\beta = 0.10$ if the degassing species is predominantly $Ge_{(g)}$, or $\beta = 0.14$ if the degassing species is predominantly $GeS_{(g)}$; and given that $\beta = \log(\alpha_k)/\log(m_{70Ge(S)}/m_{74Ge(S)})$]. Thus, kinetic Ge isotope fractionation among the IIE iron meteorites is surprisingly similar to our FeS melt degassing series performed at atmospheric pressure (i.e., $\alpha_k = 0.9942$ and $\beta = 0.15$) (Fig. 9). However, given that the IIE irons are of non-magmatic origin, constraints on the S-content of their parental melt(s) are lacking. So far, such information has only been provided for the magmatic iron meteorite groups (e.g., Chabot, 2004; Walker et al., 2008; Goldstein et al., 2009; McCoy et al., 2011; Hilton et al., 2019, 2022; Tornabene et al., 2020; Zhang et al., 2022) and, thus, the potential influence of S on the melting and degassing systematics of the IIE irons remains somewhat enigmatic. Nevertheless, from the experimental point of view alone, the Ge elemental and isotopic fractionations observed among the IIE irons would be fully consistent with (Ge) evaporation from an S-rich parental melt at pressure conditions ~1 bar.

Interestingly, kinetic Ge isotope fractionation among the IIE iron meteorites is also very similar to our Fe melt degassing series performed at low pressure conditions (i.e., 0.001 bar; $\alpha_k = 0.9940$ and $\beta = 0.11$). By contrast, the magnitude of Ge isotope fractionation inferred for our Fe melt degassing series performed at atmospheric pressure is significantly lower (i.e., $\alpha_k = 0.9971$ and $\beta = 0.05$; Fig. 9). This observation highlights that, if $Ge_{(g)}$ is the predominant degassing species of Ge in case of the IIE irons (i.e., in a low-S melt system), evaporation and loss of Ge is more likely to have occurred under low-pressure conditions. This finding would be consistent with the proposal that the IIE irons formed by near-surface melting processes induced by impacts (Wasson and Wang, 1986; Luais, 2007; Wasson, 2017; Kruijer and Kleine, 2019), and with the idea that the MVE budget of the non-magmatic IIE-group irons was established during volatile degassing processes into space under low vacuum

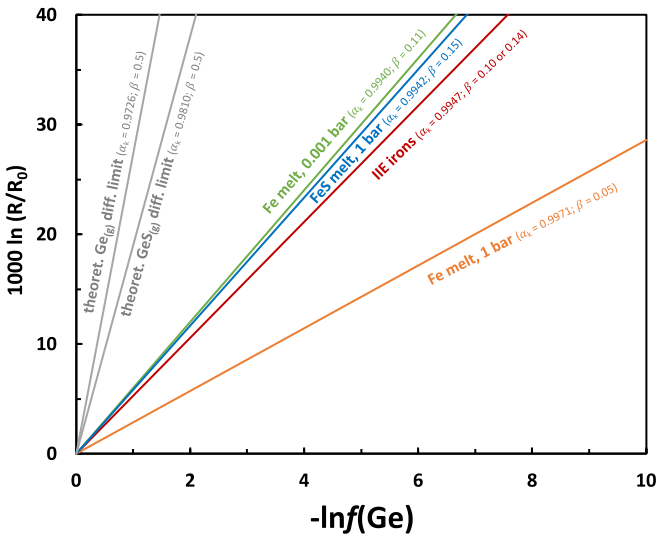

Fig. 9. Comparison of the calculated kinetic fractionation factors α_k and related β-values of the Fe metal melt degassing experiments at low vacuum (~0.001 bar; green line), Fe metal melt degassing experiments at 1 bar (orange line), FeS sulfide melt degassing experiments at 1 bar (blue line), and IIE iron meteorites (red line) in 1000ln(R/R_0) vs. –ln*f*(Ge) space. The theoretical diffusion limits of $Ge_{(g)}$ and $GeS_{(g)}$ are shown for comparison (grey lines). See Fig. 6 and Fig. 8 for details.

conditions. Of note, the sample scale of our degassing experiments is much smaller than that of actual non-magmatic iron meteorites, thus, rendering the question as to whether Ge evaporation and isotopic fractionation are limited by diffusion in the latter. However, non-polymerized metal and sulfide melts are characterized by extremely low viscosities that allow for high diffusion rates and advective and/or turbulent mixing (e.g., Terasaki et al., 2001; Sato et al., 2005). Given that non-magmatic iron meteorites are thought to have formed from relatively small melt pools and not as large planetary cores, fast homogenization of their parental melts was likely.

Overall, our experimental results demonstrate that the Ge elemental and isotopic variations among the IIE iron meteorites are well explained by evaporative Ge loss from Fe metal or FeS sulfide melts at pressure conditions ≤ 1 bar and under kinetic conditions, as simulated by our degassing experiments, therefore, supporting models proposing an origin of non-magmatic iron meteorites by near-surface impact

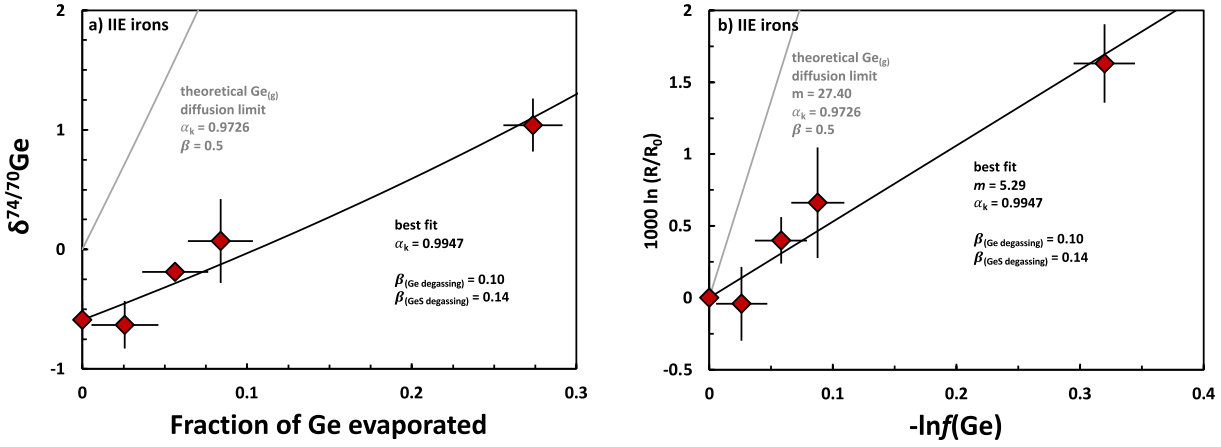

Fig. 8. (a) Germanium stable isotope fractionation as a function of Ge loss for the IIE iron meteorites. The black curve illustrates Rayleigh fractionation for evaporation of Ge and was calculated as $(\Delta^{74/70}Ge_{initial} + 1000)^*([Ge]_{residue}/[Ge]_{initial})^(\alpha_k–1)–1000$. The kinetic fractionation factor α_k was calculated from the slope m of a linear best fit of the data in 1000ln(R/R_0) vs. –ln*f*(Ge) space (panel b) as $\alpha_k = 1–m/1000$. The stated β-value is related to α_k as follows: $\beta = \log(\alpha_k)/\log(m_{70Ge(S)}/m_{74Ge(S)})$. Grey curves/lines represent theoretical limit (Graham's Law; $\beta = 0.5$; $\alpha_k = 0.9726$). Germanium concentration and isotope data for the IIE iron meteorites were taken from Luais (2007, 2012). Consequently, the inferred α_k- and β-values are similar to those obtained from the model approach of Luais (2007).

processes. As such, the MVE budgets of (at least some) early planetesimals were affected by impact-related heating and melting processes.

4.2.2. Ungrouped (non-magmatic) irons

Of the four investigated ungrouped irons of this study, Butler and NWA 859 show super-chondritic Ge/Ni, even exceeding those observed for the IAB irons (Fig. 5), indicating extreme Ge enrichments compared to the chondritic composition (Wasson, 1966, 2011). As such, Butler and NWA 859 evidently were not subject to MVE losses by degassing and will not be further discussed in the following. Nevertheless, it should be mentioned that, as for the IAB irons, their extreme enrichment in Ge is not accompanied by Ge stable isotope fractionation. In fact, even though Butler and NWA 859 are characterized by Ge concentrations four times as high as the most Ge-rich IAB irons (Choi et al., 1995; Wasson and Kallemeyn, 2002), they show quite similar $\delta^{74/70}$Ge values (e.g., $\delta^{74/70}$Ge ≈ 0.8–1.2; Luais, 2007, 2012).

By contrast, Washington County and Cambria display pronounced Ge-depletions and sub-chondritic Ge/Ni (Fig. 5). Interestingly, these two ungrouped iron meteorites are characterized by strongly fractionated Ge isotope compositions. Both samples are ~2 ‰ heavier than any other iron meteorite, ~4‰ heavier than the isotopically light IIE iron meteorite Miles (Luais 2007; Wölfer et al., 2025a), and represent the isotopically heaviest geological materials investigated so far. Given that Washington County and Cambria are ungrouped, it is not possible to determine a kinetic isotope fractionation factor for these samples in analogy to the samples of the IIE iron meteorite group. Nevertheless, the striking combination of Ge-depletions and large isotope fractionations towards heavy $\delta^{74/70}$Ge compositions suggests that the MVE budget of both samples was controlled by kinetic vaporization processes on their respective parent asteroids, potentially indicative of an impact-related origin of both samples.

In Fig. 10 we schematically illustrate the Ge elemental (i.e., Ge/Ni$_{CI}$) and isotopic compositions of Washington County and Cambria relative to potential starting compositions represented by CI chondrites (Wölfer et al., 2025b; Luais et al., 2022) and IIE iron meteorites (Luais, 2007; Wölfer et al., 2025a). In this framework, we modeled hypothetical Ge stable isotope fractionations as a function of evaporative Ge loss (i.e., decreasing Ge/Ni$_{CI}$) using different α_k. Overall, these models demonstrate that the Ge concentrations (and Ge/Ni$_{CI}$) as well as $\delta^{74/70}$Ge values of Washington County and Cambria can readily be accounted for by kinetic Ge degassing, similar to the systematics we observe for our degassing experiments and the IIE irons. This is especially true for Washington County and assuming a IIE iron-like starting composition. By contrast, assuming a CI-like starting composition, only very suppressed kinetic isotope fractionation (e.g., close to equilibrium isotope fractionation) could account for the Ge/Ni and $\delta^{74/70}$Ge compositions of Washington County and Cambria. Moreover, to explain the Ge elemental and isotopic composition of Cambria by degassing, an α_k-value closer to 1 (i.e., more suppressed Ge isotope fractionation) is required relative to the α_k-value inferred for Washington County, independent of the assumed starting composition. Nevertheless, the Ge elemental and isotopic systematics of both samples are consistent with volatility-related kinetic isotope fractionation of Ge following near-surface impact processes and, thus, with a non-magmatic origin. As such, evaporative Ge loss from Fe metal or FeS sulfide melts parental to non-magmatic iron meteorites at low pressure conditions $\leq$ 1 bar can readily account for the large Ge isotopic variations (~4‰) observed among variably Ge-depleted, non-magmatic iron meteorites.

5. Conclusions

In this study we have investigated the degassing behavior of Ge during evaporation from metal and sulfide melts in different high-temperature settings to better constrain the role of vaporization processes for setting MVE abundances in metal-bearing early Solar System materials. Our experimental results demonstrate that Ge fractionates both elementally and isotopically during evaporation from a melt, with residual run products displaying increasingly heavy Ge isotope signatures with progressive depletion of Ge, consistent with kinetic constraints (i.e., up to >30 ‰ Ge stable isotope fractionation when >99 % of the initial Ge is lost). In principle, evaporation of Ge—and consequently the magnitude of Ge isotope fractionation (i.e., $\Delta^{74/70}$Ge)—increase with increasing temperatures and decreasing pressure. Additionally, we found that the presence of S in the melt dramatically increases the evaporative loss of Ge. Ultimately, future degassing campaigns at even lower pressure conditions might be beneficial to fully understand the degassing systematics of Ge. Nevertheless, our kinetic models show that the Ge concentration and isotopic variability among samples from the non-magmatic IIE iron meteorite group can readily be explained by impact-related degassing of Ge from the surface of the IIE parent asteroid. Likewise, our new data reported for some ungrouped iron meteorites suggests that these samples also inherited their highly variable Ge elemental and isotopic compositions by evaporative loss of their MVEs and, thus, might be of non-magmatic origin (e.g., Washington

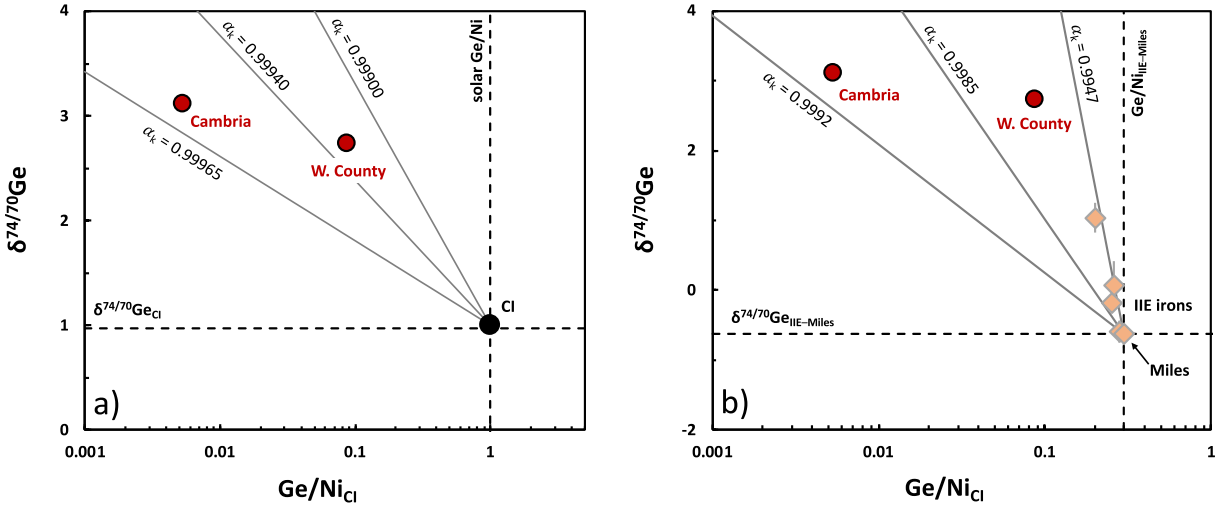

Fig. 10. Diagrams of $\delta^{74/70}$Ge vs. the CI-normalized Ge/Ni ratios of the two ungrouped, potentially non-magmatic iron meteorites Cambria and Washington County. Grey lines schematically illustrate potential Ge isotope fractionation as a function of (evaporative) Ge loss, assuming a CI chondrite-like starting composition (panel a; Wölfer et al., 2025b; Luais et al., 2022) or a IIE iron-like starting composition (panel b; Luais, 2007; Wölfer et al., 2025a), respectively, and different kinetic fractionation factors α_k.

County, Cambria). Altogether, this study attests to the importance of impact-related planetary vaporization and magma degassing processes for setting the volatile budget of (some) planetary building blocks.

Data availability

Data are available through Mendeley: https://doi.org/10.17632/km4n8m74yc.2.

CRediT authorship contribution statement

Elias Wölfer: Writing – review & editing, Writing – original draft, Visualization, Validation, Methodology, Investigation, Formal analysis, Data curation. **Christian J. Renggli:** Writing – review & editing, Validation, Supervision, Methodology, Investigation. **Christoph Burkhardt:** Writing – review & editing, Supervision, Resources, Project administration, Funding acquisition, Conceptualization. **Thorsten Kleine:** Writing – review & editing, Supervision, Resources, Project administration, Funding acquisition, Conceptualization.

Declaration of competing interest

The authors declare that they have no known competing financial interests or personal relationships that could have appeared to influence the work reported in this paper.

Acknowledgments

The degassing experiments of this study were performed at the Institute for Mineralogy at the University of Münster. We gratefully acknowledge Stephan Klemme for providing access to his experimental facilities. We also thank Frank Wombacher, Andrew M. Davis, and one anonymous reviewer for their constructive comments and Béatrice Luais for efficient editorial handling. This work was funded by the Deutsche Forschungsgemeinschaft (DFG, German Research Foundation) – Project-ID 263649064 – TRR 170 and the European Research Council Advanced Grant HolyEarth (grant no. 101019380).

References

Albarède, F., 2009. Volatile accretion history of the terrestrial planets and dynamic implications. Nature 461, 1227–1233.
Alexander, C.M.O., 2019a. Quantitative models for the elemental and isotopic fractionations in chondrites: the carbonaceous chondrites. Geochim. Cosmochim. Acta 254, 277–309.
Alexander, C.M.O., 2019b. Quantitative models for the elemental and isotopic fractionations in the chondrites: the non-carbonaceous chondrites. Geochim. Cosmochim. Acta 254, 246–276.
Alexander, C.M.O., 2005. Re-examining the role of chondrules in producing the elemental fractionations in chondrites. Meteorit. Planet. Sci. 40, 943–965.
Bourdon, B., Fitoussi, C., 2020. Isotope Fractionation during condensation and evaporation during planet formation processes. ACS Earth Space Chem. 4, 1408–1423.
Braukmüller, N., Wombacher, F., Hezel, D.C., Escoube, R., Münker, C., 2018. The chemical composition of carbonaceous chondrites: implications for volatile element depletion, complementarity and alteration. Geochim. Cosmochim. Acta 239, 17–48.
Buono, A.S., Walker, D., 2011. The fe-rich liquidus in the Fe–FeS system from 1bar to 10GPa. Geochim. Cosmochim. Acta 75, 2072–2087.
Cassen, P., 1996. Models for the fractionation of moderately volatile elements in the solar nebula. Meteorit. Planet. Sci. 31, 793–806.
Chabot, N.L., 2004. Sulfur contents of the parental metallic cores of magmatic iron meteorites. Geochim. Cosmochim. Acta 68, 3607–3618.
Choi, B.-G., Ouyang, X., Wasson, J.T., 1995. Classification and origin of IAB and IIICD iron meteorites. Geochim. Cosmochim. Acta 59, 593–612.
Corgne, A., Wood, B.J., Fei, Y., 2008. C- and S-rich molten alloy immiscibility and core formation of planetesimals. Geochim. Cosmochim. Acta 72, 2409–2416.
Dauphas, N., Schauble, E.A., 2016. Mass Fractionation Laws, mass-independent effects, and isotopic Anomalies. Annu. Rev. Earth Planet. Sci. 44, 709–783.
Davis, A.M., 2006. Volatile evolution and loss eds. D. S. Lauretta and H. Y. McSween. Meteor. Early Sol. Syst. Vol II Univ. Ariz. Press.
Escoube, R., Rouxel, O.J., Luais, B., Ponzevera, E., Donard, O.F.X., 2012. An Intercomparison study of the germanium isotope composition of geological reference materials. Geostand. Geoanalytical Res. 36, 149–159.
Florin, G., Luais, B., Alard, O., Rushmer, T., 2021. Condensation and evaporation processes during CB chondrite formation: insights from ge isotopes and highly siderophile element abundances. Meteorit. Planet. Sci. 56, 1191–1211.
Florin, G., Luais, B., Rushmer, T., Alard, O., 2020. Influence of redox processes on the germanium isotopic composition of ordinary chondrites. Geochim. Cosmochim. Acta 269, 270–291.
Goldstein, J.I., Scott, E.R.D., Chabot, N.L., 2009. Iron meteorites: crystallization, thermal history, parent bodies, and origin. Geochemistry 69, 293–325.
Grewal, D.S., Bhattacharjee, S., Zhang, B., Nie, N.X., Miyazaki, Y., 2025. Enrichment of moderately volatile elements in first-generation planetesimals of the inner solar system. Sci. Adv. 11, eadq7848.
Grossman, L., Ebel, D.S., Simon, S.B., Davis, A.M., Richter, F.M., Parsad, N.M., 2000. Major element chemical and isotopic compositions of refractory inclusions in C3 chondrites: the separate roles of condensation and evaporation. Geochimica et Cosmochimica Acta 64, 2879–2894.
Hans, U., Kleine, T., Bourdon, B., 2013. Rb–Sr chronology of volatile depletion in differentiated protoplanets: BABI, ADOR and ALL revisited. Earth Planet. Sci. Lett. 374, 204–214.
Hellmann, J.L., Hopp, T., Burkhardt, C., Kleine, T., 2020. Origin of volatile element depletion among carbonaceous chondrites. Earth Planet. Sci. Lett. 549, 116508.
Hilton, C.D., Ash, R.D., Walker, R.J., 2022. Chemical characteristics of iron meteorite parent bodies. Geochim. Cosmochim. Acta 318, 112–125.
Hilton, C.D., Bermingham, K.R., Walker, R.J., McCoy, T.J., 2019. Genetics, crystallization sequence, and age of the South Byron trio iron meteorites: new insights to carbonaceous chondrite (CC) type parent bodies. Geochim. Cosmochim. Acta 251, 217–228.
Hin, R.C., Coath, C.D., Carter, P.J., Nimmo, F., Lai, Y.-J., Pogge Von Strandmann, P.A.E., Willbold, M., Leinhardt, Z.M., Walter, M.J., Elliott, T., 2017. Magnesium isotope evidence that accretional vapour loss shapes planetary compositions. Nature 549, 511–515.
Hirschmann, M.M., Bergin, E.A., Blake, G.A., Ciesla, F.J., Li, J., 2021. Early volatile depletion on planetesimals inferred from C–S systematics of iron meteorite parent bodies. Proc. Natl. Acad. Sci. 118, e2026779118.
Hu, Y., Moynier, F., Bizzarro, M., 2022. Potassium isotope heterogeneity in the early solar system controlled by extensive evaporation and partial recondensation. Nat. Commun. 13, 7669.
Humayun, M., Clayton, R.N., 1995. Potassium isotope cosmochemistry: genetic implications of volatile element depletion. Geochim. Cosmochim. Acta 59, 2131–2148.
Jordan, M.K., Tang, H., Kohl, I.E., Young, E.D., 2019. Iron isotope constraints on planetesimal core formation in the early solar system. Geochim. Cosmochim. Acta 246, 461–477.
Klemme, S., Genske, F., Sossi, P.A., Berndt, J., Renggli, C.J., Stracke, A., 2022. Cr stable isotope fractionation by evaporation from silicate melts. Chem. Geol. 610, 121096.
Kruijer, T.S., Kleine, T., 2019. Age and origin of IIE iron meteorites inferred from hf-W chronology. Geochim. Cosmochim. Acta 262, 92–103.
Lamoreaux, R.H., Hildenbrand, D.L., Brewer, L., 1987. High-temperature vaporization behavior of oxides II. oxides of Be, Mg, Ca, Sr, Ba, B, Al, Ga, In, Tl, Si, Ge, Sn, Pb, Zn, Cd, and Hg. J. Phys. Chem. Ref. Data 16, 419–443.
Larimer, J.W., Anders, E., 1967. Chemical fractionations in meteorites—II. abundance patterns and their interpretation. Geochim. Cosmochim. Acta 31, 1239–1270.
Lodders, K., 2021. Relative atomic Solar system abundances, mass Fractions, and atomic masses of the elements and their isotopes, composition of the Solar photosphere, and compositions of the major chondritic meteorite groups. Space Sci. Rev. 217, 44.
Lord, O.T., Walter, M.J., Dasgupta, R., Walker, D., Clark, S.M., 2009. Melting in the Fe–C system to 70 GPa. Earth Planet. Sci. Lett. 284, 157–167.
Luais, B., 2012. Germanium chemistry and MC-ICPMS isotopic measurements of Fe–Ni, Zn alloys and silicate matrices: insights into deep Earth processes. Chem. Geol. 334, 295–311.
Luais, B., 2007. Isotopic fractionation of germanium in iron meteorites: significance for nebular condensation, core formation and impact processes. Earth Planet. Sci. Lett. 262, 21–36.
Luais, B., Florin, G., Cividini, D., 2022. The importance of the moderately siderophile and volatile germanium in chondrites and planetary reservoirs to reconstruct planet formation. Meteoritics Planet. Sci. 57.
McCoy, T.J., Walker, R.J., Goldstein, J.I., Yang, J., McDonough, W.F., Rumble, D., Chabot, N.L., Ash, R.D., Corrigan, C.M., Michael, J.R., Kotula, P.G., 2011. Group IVA irons: new constraints on the crystallization and cooling history of an asteroidal core with a complex history. Geochim. Cosmochim. Acta 75, 6821–6843.
Mittlefehldt, D.W., 1987. Volatile degassing of basaltic achondrite parent bodies: evidence from alkali elements and phosphorus. Geochim. Cosmochim. Acta 51, 267–278.
Neuman, M., Holzheid, A., Lodders, K., Fegley, B., Jolliff, B.L., Koefoed, P., Chen, H., Wang, K., 2022. High temperature evaporation and isotopic fractionation of K and Cu. Geochim. Cosmochim. Acta 316, 1–20.
Nie, N.X., Chen, X.-Y., Hopp, T., Hu, J.Y., Zhang, Z.J., Teng, F.-Z., Shahar, A., Dauphas, N., 2021. Imprint of chondrule formation on the K and Rb isotopic compositions of carbonaceous meteorites. Sci. Adv. 7, eabl3929.
Nielsen, S.G., Shu, Y., Wood, B.J., Blusztajn, J., Auro, M., Norris, C.A., Wörner, G., 2021. Thallium isotope Fractionation during magma degassing: evidence from experiments and Kamchatka arc lavas. Geochem. Geophys. Geosystems 22, e2020GC009608.
Norris, C.A., Wood, B.J., 2017. Earth's volatile contents established by melting and vaporization. Nature 549, 507–510.
Palme, H., O'Neill, H.St.C., 2014. Cosmochemical Estimates of Mantle Composition. In: Treatise on Geochemistry Elsevier. pp. 1–39.

Renggli, C.J., King, P.L., Henley, R.W., Norman, M.D., 2017. Volcanic gas composition, metal dispersion and deposition during explosive volcanic eruptions on the moon. Geochimica et Cosmochimica Acta 206, 296–311.
Renggli, C.J., Klemme, S., 2020. Experimental constraints on metal transport in fumarolic gases. J. Volcanol. Geotherm. Res. 400, 106929.
Renggli, C.J., Hellmann, J.L., Burkhardt, C., Klemme, S., Berndt, J., Pangritz, P., Kleine, T., 2022. Tellurium isotope fractionation during evaporation from silicate melts. Geochim. Cosmochim. Acta 339, 35–45.
Richter, F.M., Davis, A.M., Ebel, D.S., Hashimoto, A., 2002. Elemental and isotopic fractionation of type B calcium-, aluminum-rich inclusions: experiments, theoretical considerations, and constraints on their thermal evolution. Geochim. Cosmochim. Acta 66, 521–540.
Richter, F.M., Janney, P.E., Mendybaev, R.A., Davis, A.M., Wadhwa, M., 2007. Elemental and isotopic fractionation of type B CAI-like liquids by evaporation. Geochim. Cosmochim. Acta 71, 5544–5564.
Richter, F.M., Dauphas, N., Teng, F.-Z., 2009. Non-traditional fractionation of non-traditional isotopes: evaporation, chemical diffusion and soret diffusion. Chem. Geol. 258, 92–103.
Richter, F.M., Mendybaev, R.A., Christensen, J.N., Ebel, D., Gaffney, A., 2011. Laboratory experiments bearing on the origin and evolution of olivine-rich chondrules. Meteorit. Planet. Sci. 46, 1152–1178.
Rouxel, O.J., Luais, B., 2017. Germanium isotope geochemistry. Rev. Mineral. Geochem. 82, 601–656.
Sato, Y., Sugisawa, K., Aoki, D., Yamamura, T., 2005. Viscosities of Fe–Ni, Fe–Co and Ni–Co binary melts. Meas. Sci. Technol. 16, 363–371.
Scott, E.R.D., Wasson, J.T., 1975. Classification and properties of iron meteorites. Rev. Geophys. 13, 527.
Siebert, C., Nägler, T.F., Kramers, J.D., 2001. Determination of molybdenum isotope fractionation by double-spike multicollector inductively coupled plasma mass spectrometry. Geochem. Geophys. Geosystems 2, 2000GC000124.
Sossi, P.A., Klemme, S., O'Neill, H., St, C., Berndt, J., Moynier, F., 2019. Evaporation of moderately volatile elements from silicate melts: experiments and theory. Geochim. Cosmochim. Acta 260, 204–231.
Sossi, P.A., Moynier, F., Treilles, R., Mokhtari, M., Wang, X., Siebert, J., 2020. An experimentally-determined general formalism for evaporation and isotope fractionation of Cu and Zn from silicate melts between 1300 and 1500 °C and 1 bar. Geochim. Cosmochim. Acta 288, 316–340.
Spitzer, F., Burkhardt, C., Kruijer, T.S., Kleine, T., 2025. Comparison of the earliest NC and CC planetesimals: evidence from ungrouped iron meteorites. Geochim. Cosmochim. Acta, S0016703725001474.
Steenstra, E.S., Renggli, C.J., Berndt, J., Klemme, S., 2023. Evaporation of moderately volatile elements from metal and sulfide melts: implications for volatile element abundances in magmatic iron meteorites. Earth Planet. Sci. Lett. 622, 118406.
Steenstra, E.S., Renggli, C.J., Berndt, J., Klemme, S., 2024. Quantification of evaporative loss of volatile metals from planetary cores and metal-rich planetesimals. Geochim. Cosmochim. Acta 384, 93–110.
Stracke, A., Scherer, E.E., Reynolds, B.C., 2014. Application of isotope dilution in geochemistry. Treatise Geochem. Elsevier. 71–86.
Terasaki, H., Kato, T., Urakawa, S., Funakoshi, K., Suzuki, A., Okada, T., Maeda, M., Sato, J., Kubo, T., Kasai, S., 2001. The effect of temperature, pressure, and sulfur content on viscosity of the Fe-FeS melt. Earth Planet. Sci. Lett. 190, 93–101.
Tornabene, H.A., Hilton, C.D., Bermingham, K.R., Ash, R.D., Walker, R.J., 2020. Genetics, age and crystallization history of group IIC iron meteorites. Geochim. Cosmochim. Acta 288, 36–50.
Wai, C.M., Wasson, J.T., 1979. Nebular condensation of Ga, Ge and Sb and the chemical classification of iron meteorites. Nature 282, 790–793.
Walker, R.J., McDonough, W.F., Honesto, J., Chabot, N.L., McCoy, T.J., Ash, R.D., Bellucci, J.J., 2008. Modeling fractional crystallization of group IVB iron meteorites. Geochim. Cosmochim. Acta 72, 2198–2216.
Wasson, J.T., 1966. Butler, Missouri: an iron meteorite with extremely high germanium content. Science 153, 976–978.
Wasson, J.T., 2017. Formation of non-magmatic iron-meteorite group IIE. Geochim. Cosmochim. Acta 197, 396–416.
Wasson, J.T., 2011. Relationship between iron-meteorite composition and size: compositional distribution of irons from North Africa. Geochim. Cosmochim. Acta 75, 1757–1772.
Wasson, J.T., 1970. The chemical classification of iron meteorites. Icarus 12, 407–423.
Wasson, J.T., 1967. The chemical classification of iron meteorites: I. A study of iron meteorites with low concentrations of gallium and germanium. Geochim. Cosmochim. Acta 31, 161–180.
Wasson, J.T., Huber, H., Malvin, D.J., 2007. Formation of IIAB iron meteorites. Geochim. Cosmochim. Acta 71, 760–781.
Wasson, J.T., Kallemeyn, G.W., 1988. Compositions of chondrites. Philos. Trans. R. Soc. Lond. Ser. Math. Phys. Sci. 325, 535–544.
Wasson, J.T., Kallemeyn, G.W., 2002. the IAB iron-meteorite complex: a group, five subgroups, numerous grouplets, closely related, mainly formed by crystal segregation in rapidly cooling melts. Geochim. Cosmochim. Acta 66, 2445–2473.
Wasson, J.T., Schaudy, R., 1971. The chemical classification of iron meteorites—V groups IIIC and IIID and other irons with germanium concentrations between 1 and 25 ppm. Icarus 14, 59–70.
Wasson, J.T., Wang, J., 1986. A nonmagmatic origin of group-IIE iron meteorites. Geochim. Cosmochim. Acta 50, 725–732.
Wimpenny, J., Marks, N., Knight, K., Borg, L., Badro, J., Ryerson, F., 2020. Constraining the behavior of gallium isotopes during evaporation at extreme temperatures. Geochim. Cosmochim. Acta 286, 54–71.
Wimpenny, J., Marks, N., Knight, K., Rolison, J.M., Borg, L., Eppich, G., Badro, J., Ryerson, F.J., Sanborn, M., Huyskens, M.H., Yin, Q., 2019. Experimental determination of Zn isotope fractionation during evaporative loss at extreme temperatures. Geochim. Cosmochim. Acta 259, 391–411.
Wölfer, E., Burkhardt, C., Kleine, T., 2025a. Germanium stable isotope measurements by double-spike MC-ICPMS. J. Anal. at. Spectrom. 40, 1023–1036.
Wölfer, E., Burkhardt, C., Nimmo, F., Kleine, T., 2025b. Origin of moderately volatile elements in Earth inferred from mass-dependent Ge isotope variations among chondrites. Earth Planet. Sci. Lett. 663, 119435.
Wood, B.J., Smythe, D.J., Harrison, T., 2019. The condensation temperatures of the elements: a reappraisal. Am. Mineral. 104, 844–856.
Worsham, E.A., Bermingham, K.R., Walker, R.J., 2017. Characterizing cosmochemical materials with genetic affinities to the earth: genetic and chronological diversity within the IAB iron meteorite complex. Earth Planet. Sci. Lett. 467, 157–166.
Young, E.D., Galy, A., Nagahara, H., 2002. Kinetic and equilibrium mass-dependent isotope fractionation laws in nature and their geochemical and cosmochemical significance. Geochim. Cosmochim. Acta 66, 1095–1104.
Young, E.D., Shahar, A., Nimmo, F., Schlichting, H.E., Schauble, E.A., Tang, H., Labidi, J., 2019. Near-equilibrium isotope fractionation during planetesimal evaporation. Icarus 323, 1–15.
Young, E.D., Macris, C.A., Tang, H., Hogan, A.A., Shollenberger, Q.R., 2022. Isotope velocimetry: experimental and theoretical demonstration of the potential importance of gas flow for isotope fractionation during evaporation of protoplanetary material. Earth Planet. Sci. Lett. 589, 117575.
Zhang, B., Chabot, N.L., Rubin, A.E., 2022. Compositions of carbonaceous-type asteroidal cores in the early solar system. Sci. Adv. 8, eabo5781.